Comparative analyses of disease-linked missense mutations in the RNA exosome modeled in budding yeast reveal distinct functional consequences in translation

Maria C. Sterrett[1,2], Lauryn A. Cureton[3,4], Lauren N. Cohen[4], Ambro van Hoof[5], Sohail Khoshnevis[4], Milo B. Fasken[1], Anita H. Corbett[†,1], and Homa Ghalei [†,4]

[1]Department of Biology, [2]Biochemistry, Cell and Developmental Biology Graduate Program, [3]Genetics and Molecular Biology Graduate Program, Emory University, Atlanta, Georgia, USA. [4]Department of Biochemistry, Emory University School of Medicine, Atlanta, Georgia, USA. [5]Department of Microbiology and Molecular Genetics, The University of Texas Health Science Center at Houston, Houston, Texas, USA.

[†]**Corresponding authors**: Anita Corbett acorbe2@emory.edu and Homa Ghalei hghalei@emory.edu

Running title: Comparative Analysis of RNA Exosomopathy Variants

Keywords: RNA exosome, RNA exosomopathy, disease model, budding yeast disease model, translation dysregulation

ABSTRACT

The RNA exosome is an evolutionarily conserved exoribonuclease complex that consists of a 3-subunit cap, a 6-subunit barrel-shaped core, and a catalytic base subunit. Missense mutations in genes encoding structural subunits of the RNA exosome cause a growing family of diseases with diverse pathologies, collectively termed RNA exosomopathies. The disease symptoms vary and can manifest as neurological defects or developmental disorders. The diversity of the RNA exosomopathy pathologies suggests that the different missense mutations in structural genes result in distinct *in vivo* consequences. To investigate these functional consequences and distinguish whether they are unique to each RNA exosomopathy mutation, we generated a collection of *in vivo* models using budding yeast by introducing pathogenic missense mutations in orthologous *S. cerevisiae* genes. We then performed a comparative RNA-seq analysis to assess broad transcriptomic changes in each mutant model. Three of the mutant models *rrp4-G226D, rrp40-W195R* and *rrp46-L191H,* which model mutations in the genes encoding structural subunits of the RNA exosome, *EXOSC2, EXOSC3* and *EXOSC5* showed the largest transcriptomic differences. Further analyses revealed shared increased transcripts enriched in translation or ribosomal RNA modification/processing pathways across the three mutant models. Studies of the impact of the mutations on translation revealed shared defects in ribosome biogenesis but distinct impacts on translation. Collectively, our results provide the first comparative analysis of several RNA exosomopathy mutant models and suggest that different RNA exosomopathy mutations result in *in vivo* consequences that are both unique and shared across each variant, providing more insight into the biology underlying each distinct pathology.

INTRODUCTION

The steady-state state levels of cellular RNAs are regulated through a delicate balance of transcription and decay. This balance in fine-tuned through post-transcriptional events that include precise processing, decay and quality control surveillance [1]. Beyond their impact on transcriptome, the post-transcriptional regulatory events are critical to define the proteome in both time and space. The RNA exosome is an abundant, essential cellular machine that is a critical mediator of both RNA processing and decay. This macromolecular complex is composed of nine structural subunits and a catalytic 3'-5' exo-endoribonuclease (DIS3 in humans and Dis3/Rrp44 in budding yeast) [2, 3]. The subunits of the RNA exosome are highly conserved and were initially identified in *Saccharomyces cerevisiae* through a screen for ribosomal RNA processing (*rrp*) mutants [3, 4]. The structural core of the RNA exosome is composed of three S1/KH cap subunits and a lower ring of six PH-like subunits. The 3-subunit cap is composed of EXOSC1/Csl4 (Human/*S. cerevisiae*), EXOSC2/Rrp4, and EXOSC3/Rrp40. The 6-subunit core is composed of EXOSC4/Rrp41, EXOSC5/Rrp46, EXOSC6/Mtr3, EXOSC7/Rrp42, EXOSC8/Rrp43, and EXOSC9/Rrp45. The structural cap and core subunits form a barrel-like structure through which RNA can be threaded in a 5'-3' orientation. The DIS3/Dis3 or Rrp44 catalytic subunit is located at the bottom of the barrel and can process or degrade the RNA targets (**Figure 1A**). Structural studies of both yeast and human RNA exosome complexes have revealed conservation in the organization of the RNA exosome (**Figure 1B**) [2, 5-8], beyond evolutionary sequence conservation.

The RNA exosome plays a pivotal role in processing, degradation, and surveillance of nearly every class of RNA in both the nucleus and cytoplasm [9-11]. First discovered as a crucial complex required for proper maturation of ribosomal RNA [3], the RNA exosome has subsequently been shown to contribute to the processing of small nuclear RNAs (snRNAs), small nucleolar RNAs (snoRNAs) and transfer RNAs (tRNAs) [9, 12-16]. In addition, the RNA exosome is critical for RNA homeostasis within the nucleus through targeting and degrading highly unstable species, such as cryptic unstable RNAs (CUTs) in *S. cerevisiae* and promoter upstream transcripts (PROMPTs) in human cells [14, 17-20]. The RNA exosome also plays a crucial role in RNA surveillance in both the nucleus and cytoplasm,

degrading aberrant RNAs [20]. In addition to surveillance of misprocessed endogenous RNA species, the RNA exosome has been implicated in targeting foreign RNA through antiviral surveillance pathways [21].

Though the RNA exosome is essential in all cell types and models tested thus far [3, 15, 22-24], recent clinical studies have identified pathogenic missense mutations in the structural subunit genes that result in distinct tissue-specific defects comprising a growing family of diseases termed RNA exosomopathies [25]. Pathogenic missense mutations have been identified in the cap subunit genes *EXOSC1/2/3* and core subunit genes *EXOSC5/8/9* [26-37]. Missense mutations in the genes encoding the EXOSC1 and EXOSC3 cap subunit and EXOSC8 and EXOSC9 core subunits cause forms of PCH (pontocerebellar hypoplasia), a severe disease characterized by early onset atrophy of the pons and cerebellum [26, 28, 30-32, 34, 36-40]. Missense mutations in the gene encoding the EXOSC5 core subunit are linked to a disease characterized by cerebellar atrophy, SMA-like motor delays and hypotonia [33]. In contrast to most of the other mutations which primarily cause neurological defects, missense mutations in the gene encoding the EXOSC2 cap subunit are linked to a novel syndrome termed SHRF (short stature, hearing loss, retinitis pigmentosa and distinctive facies) [29]. While diverse in their clinical manifestations, typically RNA exosomopathy missense mutations result in single amino acid substitutions in conserved domains of the structural subunits of the RNA exosome.

Several recent studies have begun investigating molecular consequences of the different pathogenic amino acid substitutions that occur in exosomopathies (Summarized in **Table S1**) [41, 42]. Expression levels of EXOSC3-G31A and EXOSC3-W238R variants in a mouse neuronal line were reduced compared to wild-type mouse EXOSC3, suggesting that these amino acid substitutions could affect the stability of the subunit [41]. Additionally, analysis of PCH patient fibroblasts and skeletal muscle cells homozygous for the *EXOSC9-L14P* mutations revealed that the variant protein levels are decreased compared to EXOSC9 levels in control samples, suggesting the pathogenic substitution impacts the stability of the subunit [28]. Similarly, analyses of the EXOSC8-S272T variant in myoblasts and fibroblasts showed that the steady-state EXOSC8 level is significantly decreased compared to EXOSC8 in wild-type control cells [27]. In addition, in patient fibroblasts with mutations in *EXOSC3* and *EXOSC8*, the EXOSC9 protein level was reduced suggesting that reduced levels of one RNA exosome

subunit can destabilize the RNA exosome complex [28]. However, reconciling the diverse clinical pathologies seen in RNA exosomopathies cannot be simply explained by reductions in levels of individual essential subunits and/or the level of the RNA exosome complex. Thus, modeling these missense mutations and performing functional *in vivo* studies is critical to reveal the biology underlying RNA exosomopathy diseases.

Analysis of some of these RNA exosomopathy mutations in genetic model systems reveals distinct molecular and functional consequences resulting from the different pathogenic amino acid substitutions [33, 41-44]. These studies suggest that both complex integrity and interactions with known RNA exosome cofactors may be differentially impacted by specific RNA exosomopathy mutations [33, 41-44]. Any alteration in the RNA exosome levels or key cofactor interactions resulting from these amino acid substitutions would ultimately have an impact on the ability of the complex to process, degrade or survey RNA targets in a cell. Changes in RNA target levels could have a profound impact in certain tissues if key RNA classes or specific RNAs are misprocessed, defective RNA accumulates and/or RNA homeostasis is dysregulated. While previous studies of these RNA exosomopathy mutations provide valuable characterization *in vivo*, there has yet been a direct comparison of the defects in RNA exosome function across multiple cap and core RNA exosomopathy mutant models. A comparative assessment of how these exosomopathy amino acid substitutions affect the ability of the RNA exosome to process, degrade, and survey aberrant RNAs *in vivo* is critical to comprehensively understand the molecular consequences underlying each distinct exosomopathy disease pathology.

Here, we take advantage of the budding yeast model system to explore and compare the functional and molecular consequences of a set of pathogenic amino acid substitutions within the RNA exosome. Given that the RNA exosome was initially identified and has been most extensively studied in *Saccharomyces cerevisiae* [3, 45] and the high conservation in overall complex structure between the human and budding yeast RNA exosomes [28, 46, 47], a budding yeast system provides a robust platform to comparatively assess the *in vivo* consequences of exosomopathy mutations. In this study, we generated and analyzed *S. cerevisiae* models of the exosomopathy amino acid changes identified in *EXOSC2*, *EXOSC3*, *EXOSC5*, and *EXOSC9* by mutating the corresponding budding yeast genes *RRP4*,

RRP40, *RRP46* and *RRP45.* We analyzed yeast cell growth and employed an unbiased RNA-seq approach to explore the consequences of these missense mutations. From these approaches, we detect the greatest functional defects in three of our mutant models, *rrp4-G226D, rrp40-W195R* and *rrp46-L191H*. Comparative analysis of transcriptomes across these three models revealed some shared changes, particularly in coding and non-coding transcripts required for rRNA processing and ribosome biogenesis, suggesting potential defects in translation. We also identified differentially expressed genes that are unique to each of the three mutant models, suggesting that while there are some shared consequences there are also distinct differences in RNA exosome function. Assessment of ribosome biogenesis and translation defects in the three models revealed shared defects in rRNA processing, but distinct differences in polysome profiles and translation fidelity. Our results represent an unbiased approach to comparatively characterize the molecular defects in the function of the RNA exosome across a collection of RNA exosomopathy mutant models and suggest distinct translational defects may underlie the unique molecular pathology of RNA exosomopathies.

RESULTS

RNA exosomopathy mutations modeled in *Saccharomyces cerevisiae* cause different growth phenotypes.

To perform *in vivo* functional studies, we employed the budding yeast model system to assess the differential consequences resulting from each RNA exosomopathy mutation. As shown in **Figure 1C**, the residues that are substituted in RNA exosomopathy patients are highly conserved, allowing for the variant to be readily modeled in *S. cerevisiae.* One RNA exosomopathy-linked mutations identified in the cap subunit gene *EXOSC2* result in amino acid substitution Gly198Asp (G198D) [29] and in *EXOSC3* amino acid substitutions Asp132Ala (D132A) and Trp238Arg (W238R) [30, 31, 48, 49]. These amino acid variants occur in highly conserved domains of both cap subunits in similar regions, with EXOSC2-G198A and EXOSC3-W238R within or flanking a conserved structural “GxNG” motif within the RNA binding KH domain. The RNA exosomopathy-linked missense mutations identified in the core subunit genes

EXOSC5 and *EXOSC9* also result in amino acid substitutions in conserved domains of each protein. Mutations in *EXOSC5* result in amino acid changes Thr114Ile (T114I), Met148Thr (M148T), and Leu206His (L206H). These residues are located throughout the PH domain of the core subunit, however the EXOSC5-L206 falls close to the C-terminal end of the protein. Similarly, the EXOSC9 RNA exosomopathy pathogenic substitution falls near the end of the protein. The RNA exosomopathy mutation in *EXOSC9* results in Leu14Pro (L14P) located near the N-terminus of the protein. Structural analysis of each RNA exosomopathy amino acid substitution suggests that these changes could affect inter-subunit binding interfaces or the conformation of the subunits themselves [6, 25, 33, 41, 43].

We modeled the RNA exosomopathy mutations found in *EXOSC2/3/5/9* in the corresponding *S. cerevisiae* genes *RRP4/40/46/45* to produce budding yeast subunit variants containing the pathogenic amino acid substitutions. The SHRF-linked *EXOSC2 G198D* mutation is modeled by the *rrp4-G226D* yeast cells. The PCH-linked *EXOSC3-D132A, EXOSC3-W238R* and *EXOSC9-L14P* mutations are modeled by the *rrp40-S87A, rrp40-W195R* and *rrp45-I15P* yeast cells, respectively. The *EXOSC5* RNA exosomopathy mutations *EXOSC5-T114I, EXOSC5-M148T* and *EXOSC5-L206H* are modeled by the *rrp46-Q86I, rrp46-L127T,* and *rrp46-L191H* yeast cells. We first performed plasmid shuffling in cells that were deleted for the genomic *RRP* gene (*rrp4Δ, rrp40Δ, rrp45Δ* and *rrp46Δ)* and transformed with plasmids containing the different variant alleles. We then assessed the function consequences of each RNA exosomopathy mutant model by performing a growth assay on solid minimal media. We also included the parental wild-type budding yeast strain (*BY4741)* within these experiments as an isogenic control for the genetic background of the *rrp4Δ, rrp40Δ, rrp45Δ* and *rrp46Δ* cells. Control cells expressing *RRP4, RRP40, RRP45* and *RRP46* grew like parental control cells at both 30°C and 37°C (**Figure 2A**).

Previous work has characterized the functional consequences of the *rrp4, rrp40* and *rrp46* mutant models [33, 41, 43]. In particular, these previous studies showed that the *rrp4-G226D, rrp40-W195R* and *rrp46-L191H* alleles can replace the essential *RRP* genes and that they each cause growth defects compared to the corresponding wild-type control [33, 41, 43]. Consistent with these results, the *rrp4-G226D, rrp40-W195R* and *rrp46-L191H* mutant cells show slower growth at 30°C and 37°C compared to corresponding wild-type controls (**Figure 2A**). Notably, the *rrp4-G226D* cells show the most severe

growth defect at 37°C. Furthermore, the *rrp40-S87A, rrp46-Q86I* and *rrp46-L127T* cells show no growth defects compared to the wild-type control *RRP40* or *RRP46* cells (**Figure 2A**). Similar to these mutant models, the *rrp45-I15P* cells show no difference in growth compared to *RRP45* wild-type control cells or the parental control cells (**Figure 2A**). We also included *rrp6Δ* cells which lack the RNA exosome cofactor Rrp6 as a comparative control for cells with disrupted RNA exosome function. The Rrp6 exonuclease is non-essential however the cofactor assists the RNA exosome in targeting and degradation of several key transcript RNAs [7, 50-52]. As expected from previous work [50], the *rrp6Δ* cells show extremely poor growth at 37°C compared to control cells. In comparing this impaired growth phenotype to the slower growing RNA exosomopathy mutant models, the *rrp4-G226D* cells appear most similar in growth to *rrp6Δ* cells (**Figure 2A**).

We also quantified the doubling time of this collection of RNA exosomopathy mutant cells at 30°C (**Figure 2B**) and 37°C (**Figure 2C**) in liquid media. Consistent with the solid media growth assays, the *RRP* wild-type control cells have doubling times similar to the parental control cells at both 30°C and 37°C. The *rrp4-G226D, rrp40-W195R* and *rrp46-L191H* cells display significantly increased doubling times compared to control cells at both 30°C and 37°C. At 30°C, the *rrp46-L191H* cells have the longest doubling time, almost mirroring the doubling time measured for the *rrp6Δ* cells. However, at 37°C, the *rrp4-G226D* cells have the longest doubling time, comparable to that observed for the *rrp6Δ* cells. Overall, these data suggest that RNA exosomopathy mutations affecting different subunits of the RNA exosome have varied functional consequences *in vivo* with most significant growth defects observed for *rrp4-G226D, rrp40-W195R* and *rrp46-L191H.* These three modeled mutations have been shown previously to have varying impact on the protein levels of the individual yeast RNA exosome subunits [33, 41, 43], with the Rrp40 W195R variant showing the largest amount of protein instability at both 30°C and 37°C [53]. Given the *rrp40-W195R* cells show the mildest growth defect compared to the *rrp4-G226D* and *rrp46-L191H* cells relative to each corresponding control wild-type cell, these data suggest that the observed growth defects are not simply due to varying levels of loss of the essential subunits and subsequent loss of the complex. Thus, these *S. cerevisiae* models can be used to comparatively

assess the molecular consequences that may arise in the processing and/or degradation of RNA from these RNA exosomopathy mutations.

The Rrp4-G226D, Rrp40-W195R and Rrp46-L191H variants cause broad transcriptomic changes.

To achieve an unbiased investigation of the molecular consequences of the modeled RNA exosomopathy pathogenic amino acid substitutions, we performed RNA-seq analysis on three independent biological replicates of the mutant models, *rrp4-G226D*, *rrp40-S87A*, *rrp40-W195R, rrp45-I15P, rrp46-Q86I*, *rrp46-L127T,* and *rrp46-L191H* and their corresponding wild-type controls. The genetic background for all mutants and their corresponding wild-type controls are identical, thus allowing comparative analyses across the models and ensuring that observed differences from the RNA-seq analysis can be attributed to the modeled pathogenic amino acid substitution. To identify transcripts that are differentially expressed, we performed differential expression analysis on each mutant compared to its corresponding wild-type control. This analysis revealed the *rrp4-G226D, rrp40-W195R* and *rrp46-L191H* cells have a large number of transcripts differentially increased or decreased compared to their corresponding control cells (**Figure 3A**). Unbiased principal component analyses (PCA) of the RNA-seq data revealed reproducibility amongst the RNA-seq biological replicates and confirmed that the *rrp4-G226D*, *rrp40-W195R* and *rrp46-L191H* transcriptomes are distinct from those of their wild-type controls (**Figure S1**).

Differential gene expression analysis of the *rrp4-G226D* cells reveals 516 decreased transcripts (Fold change(FC) ≤-1.5, $p<0.05$) and 1196 increased transcripts (FC≥1.5, $p<0.05$) compared to the control (**Figure 3B**). Most decreased transcripts are mRNAs (87%) (**Figure 3C**), with the most significantly decreased transcript (FC≤-3) being *SSA1,* an mRNA that encodes a member of the Hsp70 chaperone family [54-56]. Interestingly, several other transcripts that encode heat shock protein family members are significantly decreased in *rrp4-G226D* cells, including *SSA2* (FC≤-3 FC), a paralog of *SSA1* [56, 57], *HSC82* (FC≤-3 FC) [58, 59], and *HSP60* (FC≤-2) among others. Some of the most significantly decreased transcripts in *rrp4-G226D* cells are *RPS3* (FC≤-2) and *RPL15A* (FC≤-2), which encode protein components of the small and large ribosomal subunit, respectively [60]. The decrease of

these ribosomal protein encoding transcripts is consistent with previous RNA-seq analysis performed on *rrp4-G226D* cells [43]. In contrast, only ~20% of the increased transcripts are mRNAs, with the majority of increased transcripts being cryptic unstable transcripts (CUTs), stable unannotated transcripts (SUTs), or other ncRNAs (**Figure 3C**). The most significantly increased transcripts are two mRNAs, *PIR3* (FC≥3) and *DDR2* (FC≥4). *PIR3* encodes for an O-glycosylated cell wall protein that is required for cell wall stability [61] and *DDR2* encodes a multi-stress response protein [62].

Differential gene expression analysis of the *rrp40-W195R* cells reveals 426 decreased transcripts (FC≤-1.5, p<0.05) and 569 increased transcripts (FC≥1.5, p<0.05) compared to the *RRP40* control (**Figure 3D**). Over 80% of the 426 decreased transcripts are mRNAs (**Figure 3E**), with the most significantly decreased transcripts being mRNAs involved in metabolic and biomolecular synthesis pathways including *URA1* and *URA4* (FC≤-3), which encode enzymes that catalyzes the steps in *de novo* synthesis of pyrimidines [63], *MDH2* (FC≤-3), which encodes a cytoplasmic malate dehydrogenase [64], and *HIS4* (FC≤-4), which encodes a multifunctional enzyme involved in histidine biosynthesis [65]. Among the most significantly decreased transcripts in *rrp40-W195R* cells are mRNAs *RPS13* (FC≤-2) and *RPS7B* (FC≤-2), encoding components of the small and large ribosomal subunit, respectively [60]. Of the 569 increased transcripts, the majority are ncRNAs such as CUTs (29.15%), SUTs (15.02%), snoRNAs (5.30%) and tRNAs (5.83%) (**Figure 3E**). Many of the most significantly increased transcripts in *rrp40-W195R* cells are uncharacterized ORFS and ncRNAs, with snoRNAs *snR66* and *snR65* among the most significantly increased transcripts detected (FC≥3). As observed in the *rrp4-G226D* transcriptome, only ~20% of transcripts significantly increased in *rrp40-W195R* cells are mRNAs.

Differential gene expression analysis of the *rrp46-L191H* cells reveals 487 decreased transcripts (FC≤-1.5, p<0.05) and 724 increased transcripts (FC≥1.5, p<0.05) compared to the control (**Figure 3F**). Of the 487 decreased transcripts, ~60% are mRNAs while the others are ncRNAs, with nearly 10% being tRNAs, and a combined ~20% being CUTs, SUTs and uncharacterized/dubious ORFs (**Figure 3G**). The

most significantly decreased transcripts in *rrp46-L191H* cells are mRNAs involved in biomolecular synthesis pathways, including *HIS4* (FC≤-4) [65], *URA1* and *URA4* (FC≤-2) [63], *BIO3* and *BIO4* (FC≤-4) [67, 68], and *RIB4* (FC≤-3) [69]. As observed for the *rrp4-G226D* cells, two of the most significantly decreased transcripts in *rrp46-L191H* cells are *RPS3* and *RPL15A* mRNAs (FC≤-2). Of the 724 increased transcripts, ~30% are classified as CUTs, ~15% classified as SUTs and ~30% are mRNAs (**Figure 3G**). The most significantly increased transcripts are *RPL18B* (FC≥3), which encodes a component of the large ribosomal subunit [60], and *CBT1* (FC≥4) which encodes a protein involved in 5' RNA end processing of mitochondrial cytochrome *b* mRNA [70] and also linked to processing of 15S rRNA [71].

Visualizations of the differential expression analyses for the *rrp40-S87A, rrp45-I15P*, *rrp46-Q86I* and *rrp46-L127T* transcriptomes are presented in **Figure S2** and reveal minor differential expressions. Overall, the differential expression analyses show broad transcriptomic changes in the *rrp4-G226D, rrp40-W195R* and *rrp46-L191H* cells that can partially explain the growth defects observed in these cells. These broad transcriptomic changes also reflect defects in the function of the RNA exosome. Consistent with the role the RNA exosome plays in degradation of nascent ncRNA species, the CUTs and SUTs combined make up the largest group of transcripts significantly increased in *rrp4-G226D, rrp40-W195R* and *rrp46-L191H* cells (**Figure 3**). As CUTs and SUTs are stabilized in RNA exosome mutants and crosslink to the RNA exosome [14, 18, 61, 62], these transcripts are likely direct targets of the RNA exosome and the observed increase is indicative of disrupted function of the complex. This significant increase in CUTs and SUTs is also consistent with previous RNA-seq analysis of the *rrp4-G226D* cells [43].

Comparison across the *rrp4-G226D, rrp40-W195R* and *rrp46-L191H* mutant models is intriguing when the overall classes of RNAs that are significantly increased or decreased are considered (**Figures 3C**, **3E** and **3G**). The majority of transcripts decreased in all three mutants are mRNAs. However, in the *rrp46-L191H* mutant, only 58% of the significantly decreased transcripts are mRNAs, as compared to 80-

90% in both the *rrp4-G226D* and *rrp40-W195R* cells. In the *rrp46-L191H* cells, nearly 10% of decreased transcripts are tRNAs and 10% are CUTs and SUTs. In the *rrp4-G226D* cells, ~5% of decreased transcripts are tRNAs, but the level of decreased CUTs and SUTs is much lower. This decrease in tRNAs is not shared in the *rrp40-W195R* cells, which only show 0.23% of decreased transcripts that are tRNAs. These divergent changes are even more apparent when we compare the categories of significantly increased transcripts. While there is an increase in CUTs and SUTs across all three mutant models, these non-coding transcripts comprise different percentages of the transcripts affected in each mutant strain. In particular, the *rrp4-G226D* cells have the largest percentage of SUTs increased of the three mutants. There are also distinct increases in other ncRNAs across the three mutants, including snoRNAs and tRNAs. The *rrp40-W195R* cells show the highest level of differentially increased snoRNAs (5.3%) and tRNAs (5.8%) among the three mutants. In summary, the *rrp4-G226D, rrp40-W195R* and the *rrp46-L191H* cells have distinct transcriptomic changes as compared to corresponding wild-type control cells and these changes also differ among the three mutants, suggesting differential consequences resulting from the RNA exosome variants *in vivo.*

Comparative assessment of differentially expressed transcripts within *rrp4-G226D, rrp40-W195R* and *rrp46-L191H* mutants suggests shared impacts on metabolic pathways and rRNA modification and processing.

To further compare the molecular consequences resulting from the modeled RNA exosomopathy mutations, we investigated what decreased and increased transcripts were shared across the *rrp4-G226D, rrp40-W195R* and *rrp46-L191H* models. To do so, we generated UpSet plots on lists of differentially expressed transcripts that were significantly decreased (FC≤-1.5, $p<0.05$) or increased (FC≥ +1.5, $p<0.05$) within the three mutant models (**Figure 4**). From the UpSet plot, we identified 209 significantly increased transcripts (FC≥ +1.5, $p<0.05$) that are shared across the *rp4-G226D*, *rrp40-W195R* and *rrp46-L191H* models (**Figure 4A**). Of the 209 transcripts increased, a majority are CUTs and SUTs, consistent with the trend observed for each *rrp* mutant model (**Figure 4B**). GO analysis on these increased transcripts revealed that rRNA modification (GO:0000154) is the most significant biological

process enriched (**Figure 4C**). This GO analysis result likely reflects the 5.8% of the 209 increased transcripts that are snoRNAs, which are required for rRNA modifications. Surprisingly, sexual sporulation (GO:0034293) and meiotic cell cycle (GO:0051321) are also two significantly enriched biological processes within these shared increased transcripts. Overall, the significant enrichment among the three mutant models in rRNA modification (GO:0000154), rRNA methylation (GO:00031167) and rRNA processing (GO:0006364) (**Figure 4C**) strongly suggests significant impacts on ribosome biogenesis within these models. We also detected 86 transcripts shared that are significantly decreased (**Figure 4D**) among the *rrp4-G226D, rrp40-W195R* and the *rrp46-L191H* cells. Of these 86 decreased transcripts, 89.5% are mRNAs (**Figure 4E**). Gene Ontology (GO) analysis on these 86 shared decreased transcripts revealed metabolic and biosynthetic biological processes as the top significantly impacted, with carboxylic acid (GO:0019752), oxoacid metabolic (GO:0043436), and organic acid metabolic process (GO:0006082) the most significantly enriched processes (**Figure 4C**).

To further assess shared changes, we performed GO analyses on the identifiable human homologs of the shared 209 increased transcripts and 86 decreased transcripts (**Supplementary Documentation S1).** Of the shared 206 increased transcripts, few had identifiable human homologs as a majority are yeast-specific CUTs and SUTs. GO analysis of those transcripts that had identifiable human homologs reveals a significant enrichment in synaptic vesicle priming and fusion biological processes (GO:0016082; GO:0031629; GO:0099500). The same GO biological processes most significantly enriched in the shared 86 decreased budding yeast transcripts, carboxylic acid (GO:0019752), oxoacid metabolic (GO:0043436), and organic acid metabolic process (GO:0006082), are the most significantly enriched processes for the identified human homologs. This analysis suggests that the modeled RNA exosomopathy mutations result in changes in highly conserved metabolic and biosynthetic pathways.

In comparing mutant models two by two, we identified shared transcripts that are significantly increased in mutant pairs: 54 in *rrp40-W195R* and *rrp46-L191H* cells, 152 in both *rrp40-W195R* and *rrp4-G226D* cells, and 268 in *rrp4-G226D* and *rrp46-L191H* cells (**Figure S3A**). Most increased transcripts shared between *rrp40-W195R* and *rrp46-L191H* are mRNAs (**Figure S3B**). GO analysis on the 54 transcripts shared between *rrp40-W195R* and *rrp46-L191H* cells revealed a significant enrichment in

rRNA metabolic process (GO:0016072), ncRNA processing (GO:0034470), rRNA processing (GO:0006364) and ribosome biogenesis (GO:0042254) (**Figure S3C**). Interestingly, however, classification of the 152 shared transcripts that are significantly increased in both *rrp40-W195R* and *rrp4-G226D* cells modeling mutations in cap RNA exosome subunits, revealed that only a portion of those changed are mRNAs, with a larger majority being non-coding CUTs and SUTs (**Figure S3B**). GO analysis of these 152 shared transcripts revealed no significant enrichment of any biological process. Classification of the 268 shared transcripts that are significantly increased in *rrp4-G226D* and *rrp46-L191H* cells also revealed a majority are CUTs and SUTs (**Figure S3B**).

We also identified 97 shared transcripts in *rrp40-W195R* and *rrp46-L191H* cells, 100 shared transcripts in *rrp40-W195R* and *rrp4-G226D* cells, and 50 shared transcripts in *rrp4-G226D* and *rrp46-L191H* cells that were significantly decreased (**Figure S3E**). Most of the decreased transcripts shared between paired groups are mRNAs (**Figure S3F**). Intriguingly, a large percentage of shared transcripts that are significantly decreased in the *rrp4-G226D* and *rrp46-L191H* cells are tRNAs (**Figure S3F**). GO analyses on the shared transcripts between paired groups reveal enrichment in different biological processes related to translation. A significant number of the 100 shared transcripts significantly decreased in both *rrp4-G226D* and *rrp40-W195R* cells impact cytoplasmic translation (GO:0002181) (**Figure S3G**). A significant number of the 50 shared transcripts significantly decreased in both *rrp4-G226D* and *rrp46-L191H* cells impact translation elongation (GO:0006414) (**Figure S3H**), consistent with the large percentage of tRNAs that are decreased in both models. No significant enrichment of any specific biological process was detected for the 97 shared transcripts significantly decreased in the *rrp40-W195R* and *rrp46-L191H* cells. Both GO analyses of the shared increased transcripts between *rrp4-G226D* and *rrp40-W195R* and *rrp40-W195R* and *rrp46-L191H* also reveal significant enrichment of biosynthetic processes, such as amide biosynthesis (GO:0043604), organonitrogen compound biosynthesis (GO:1901566) and cellular macromolecule biosynthesis (GO:0034645). In summary, transcripts from pathways related to ribosome biogenesis appear to be significantly enriched across all three mutants, consistent with the major role of RNA exosome in rRNA processing. The *rrp40-W195R* and *rrp4-G226D* cells, modeling mutations in the cap subunit genes, show different shared targets with

the *rrp46-L191H* cells, modeling a mutation in a core subunit gene, suggesting that the type of RNA exosome subunit that is mutated influences the different RNA classes that are specifically impacted by each mutant.

Comparative assessment of differentially expressed transcripts specific to *rrp4-G226D, rrp40-W195R* or *rrp46-L191H* suggest impacts on translation and ribosome biogenesis.

In examining unique transcriptomic changes, we identified transcripts that are significantly increased specifically in each mutant model; 154 in the *rrp40-W195R* cells, 193 in the *rrp46-L191H* cells and 567 in the *rrp4-G226D* cells (**Figure 5A**). Analysis of these individual sets of changes revealed a divergent pattern between the three mutant models (**Figure 5B**). Of the 154 transcripts that are increased specifically in the *rrp40-W195R* cells, nearly a quarter are snoRNAs, snRNAs, and tRNAs. Another quarter of these 154 transcripts are CUTs and SUTs, a third quarter are mRNAs, and the fourth quarter mostly dubious or uncharacterized open reading frames (ORFs). Intriguingly, the transcripts increased only in *rrp46-L191H* cells show a different pattern, with a large majority of those 193 RNAs consisting of mRNAs. Lastly, the *rrp4-G226D*-specific increased RNAs show yet a different pattern, with a majority being CUTs and SUTs. GO analysis of the 154 transcripts significantly increased in only the *rrp40-W195R* cells revealed significant enrichment in biological processes involved in gene expression (GO:0010467), rRNA modification (GO:00000154), and translation elongation (GO: 0006414) (**Figure 5C**). GO analysis of the 193 transcripts increased specifically in the *rrp46-L191H* cells revealed significant enrichment in processes related to ncRNA processing (GO:0034470) and ribosome biogenesis (GO:0042254) (**Figure 5D**). GO analysis of the transcripts increased only in the *rrp4-G226D* cells revealed no significant enrichment, likely due to the large percentage of CUTs and SUTs.

We also identified 143 transcripts that are significantly decreased specifically in the *rrp40-W195R* cells, 254 transcripts significantly decreased specifically in the *rrp46-L191H* cells, and 280 transcripts significantly decreased specifically in the *rrp4-G226D* cells (**Figure 5E**). From this analysis, distinct patterns emerge comparing the core subunit *rrp46-L191H* mutant and the cap mutant models *rrp4-G226D* and *rrp40-W195R* (**Figure 5F**). Most transcripts decreased specifically in either of the cap mutant

models are mRNAs, while more diverse transcript types are impacted in the *rrp46-L191H* cells with about a third comprised of tRNAs, CUTs and SUTs (**Figure 5F**). GO analysis of the 143 transcripts that are decreased specifically in the *rrp40-W195R* revealed significant enrichment in biological processes related to cytoplasmic translation (GO:0002181) and ribosomal small subunit assembly (GO:0000028) (**Figure 5G**). GO analyses of the 254 transcripts decreased specifically in the *rrp46-L191H* cells and the 280 transcripts decreased specifically in the *rrp4-G226D* cells also show significant enrichment in processes related to translation (GO:0006412) as well as amide and peptide biosynthesis and metabolic processes (**Figure 5H-I**).

Overall, the GO analyses performed on the transcripts changed solely in each mutant model revealed enrichment in several similar biological processes, particularly those related to ribosome biogenesis, translation and biosynthesis. However, the transcripts used to produce the GO terms in **Figure 5** are significantly changed specifically within each cell type—*rrp4-G226D, rrp40-W195R* or *rrp46-L191H*. Therefore, while there may be overlapping impacts on key biological processes within each cell type, these consequences are in part due to distinct targets.

Differential accumulation of CUTs and SUTs between RNA exosomopathy mutant models suggests functional defects in RNA exosome function.

A critical role of the RNA exosome in *S. cerevisiae* is the targeting and degradation of CUTs and SUTs ncRNA species. RNA-seq analysis of *rrp4-G226D, rrp40-W195R* and *rrp46-L191H* revealed accumulation of CUTs and SUTs, with these classes being the predominate type of RNA significantly increased across all three yeast cells. Currently there is no GO annotation associated with budding yeast CUTs and SUTs, therefore the GO analyses presented do not include these transcripts. To comparatively evaluate CUTs and SUTs changes across the three *rrp* mutant models, we generated a heatmap of normalized FPKM expression estimates to compare the impact these *rrp* mutations have on the CUTs and SUTs (**Figure S4**). We included FPKM estimates of the *rrp6*Δ samples as these transcripts were first identified by deletion of *RRP6* and Rrp6 activity is important for degradation of the CUTs [61, 63, 64]. The *rrp6*Δ samples show a broad, indiscriminate increase in all CUTs and SUTs

(**Figure S4**). A broad increase in CUTs and SUTs is also detected in the *rrp4-G226D* cells with the triplicates clustering together, separately from the other *rrp* mutant samples. The *rrp40-W195R* and *rrp46-L191H* expression data also show an increase of CUTs and SUTs, though not as broad an effect as observed in the *rrp4-G226D* cells (**Figure S4**). This overall increase across the three *rrp* mutant models can be interpreted as disrupted RNA exosome targeting and function. However, the heatmap presented in **Figure S4** shows that not all the same CUTs and SUTs are changed in *rrp4-G226D*, *rrp40-W195R* and *rrp46-L191H* cells. While the *rrp4-G226D* cells show the broadest increase in CUTs and SUTs of the three RNA exosomopathy mutant models assessed, there are definitive groups of CUTs and SUTs that appear to not be increased. Similarly, *rrp40-W195R* and *rrp46-L191H* show some shared and some distinct changes in CUTs and SUTs. These observations suggest that within *rrp4-G226D, rrp40-W195R* and *rrp46-L191H* yeast cells, RNA exosome targeting and degradation is impacted, yet in distinct ways, as all targets are not indiscriminately elevated across the three mutant models.

RNA exosomopathy yeast mutant models cause defects in ribosome biogenesis, impact global translation, and alter translational fidelity.

The most abundant cellular transcripts, rRNAs, are targeted by the RNA exosome for processing. Within the presented GO analyses performed on the RNA-seq data from *rrp4-G226D, rrp40-W195R* or *rrp46-L191H*, many common GO terms enriched are related to translation and ribosome biogenesis. Differential expression analysis revealed that some of the most significantly decreased transcripts in all three *rrp* mutant models were *RPS* and *RPL* mRNAs which encode components of the ribosome [60]. To broadly compare impacts on ribosomal protein genes across the *rp4-G226D, rrp40-W195R* and *rrp46-L191H* models, we generated heatmaps of normalized FPKM expression estimates specifically for the *RPS* and *RPL* genes (**Figure S5**). We included FPKM estimates for *rrp6*Δ cells that were collected in the same RNA-seq experiment. Consistent with previous work, there is a broad decrease in transcript levels for most ribosomal protein genes in *rrp6*Δ samples [65]. Furthermore, we detect an overall decrease in ribosomal protein gene transcripts in the three RNA exosomopathy models with the triplicates clustering together, though the magnitude of the decrease is less than the decrease observed in the *rrp6*Δ

samples. Interestingly, the *rrp4-G226D* samples show the broadest decrease in expression of ribosomal protein transcripts compared to the *rrp40-W195R* and *rrp46-L191H* samples, with the three triplicates clustering together, separate from the other *rrp* mutant samples. The *rrp40-W195R* samples show the smallest change in expression levels of *RPS* and *RPL* transcripts, with one of the triplicates clustering with the wild-type controls.

In order to further assess the impacts on ribosomal biogenesis within these three *rrp* mutant models, we performed northern blots to reveal changes in rRNA processing among the mutant models (**Figure S6A**). Consistent with previously published data [42, 43], quantification of northern blots for 2-3 biological replicates of each mutant cell showed that *rrp4-G226D* and *rrp40-W195R* cells both had significant accumulation of 7S pre-rRNA, a precursor of mature 5.8S rRNA that is processed by the RNA exosome (**Figure 6A**). The magnitude of 7S accumulation was higher for *rrp4-G226D* cells, consistent with the more severe growth defect of these cells compared to the other two mutants. The three mutant models also show significant reduction of the mature 18S, 25S, and 5.8S rRNAs (**Figure 6A**), which are processed from a polycistronic early rRNA precursor transcript (**Figure S6B**). In line with these results, global translation was significantly lower in RNA exosomopathy mutant yeast models as evident by the lower incorporation rate of L-homopropargylglycine (HPG) into the nascent polypeptide chains in actively growing mutant cells compared to the wild-type control (**Figure S7**). Collectively, these results demonstrate a global reduction in translation for all three of these RNA exosomopathy yeast mutants compared to wild-type control cells.

To test whether translation by fewer ribosomes in RNA exosomopathy mutant cells impacts protein homeostasis, we assayed translational fidelity using previously established dual-luciferase reporters [66-68]. In these plasmids, Renilla luciferase is constitutively expressed whereas the production of firefly luciferase is dependent on a translational fidelity defect such as a programmed frameshifting event, recognition of an alternative start site or miscoding. Interestingly, the *rrp4-G226D* and *rrp40-W195R* cells show a statistically significant decrease in decoding the H245R near-cognate mutant firefly luciferase mRNA compared to wild-type control (**Figure 6B**). This decoding defect could be indicative of decreased rates of translation elongation in cap RNA exosomopathy yeast mutant cells, e.g., due to

relative changes in tRNA abundances, which likely provides more time for discrimination between aminoacyl tRNAs [69]. In summary, these results indicate a severe defect in translation in RNA exosomopathy yeast mutant models that correlates with the type of RNA exosome subunit that is changed, i.e., cap vs core subunit.

Translation differences assayed by polysome profiling suggest distinct molecular consequences in ribosome pools between cap and core RNA exosomopathy mutations.

To explore specific translational differences arising from distinct transcript changes in mutant cells, we performed polysome profiling. For this assay, we used CRISPR/Cas9-edited *rrp4-G226D*, *rrp40-W195R*, and *rrp46-L191H* mutant cells. The cell phenotypes were assessed for temperature-sensitive growth on solid media and rescue of the growth of the mutant cells by wild-type *RRP4*, *RRP40*, and *RRP46* plasmids compared to the wild-type *BY4741* parental cells was determined (**Figure S8**). As expected from cells with reduced mature rRNAs, all three mutant cells show a significant decrease in the level of polysomes compared to wild-type control cells (**Figure 7A**). In addition, the cap subunit mutant cells show an accumulation of halfmer polysomes, evident as shoulders on the 80S monosome peak in the *rrp4-G226D* cells and on the monosome, disome and trisome peaks in the *rrp40-W195R* cells, not found in the profiles from the wild-type or *rrp46-L191H* core subunit mutant cells (**Figure 7A**). The halfmers could form due to inefficient subunit joining during translation initiation because of defects/reduction in biogenesis or stability of 60S subunits compared to 40S. Indeed, the polysome profiles of the cap subunit mutants show a significantly higher ratio of free 40S to free 60S peak, which is not observed in the polysome profile of the core subunit mutant where halfmers are not produced. Thus, the translating ribosome pool in the cap vs core mutant yeast cells is distinctly different.

The Rrp4-G226D variant has decreased association with the essential helicase Mtr4 [43]. Previous work has shown that a temperature-sensitive mutant of *MTR4* results in escape of 7S pre-rRNA-containing ribosomes into pool of translating ribosomes [70]. To assess whether and how RNA exosomopathy yeast models affect the quality of translating ribosomes, we assayed the distribution of 7S pre-rRNA in polysome fractions of mutant cells compared to control wild-type cells (**Figure 7B**). In wild-

type cells, 7S pre-rRNA peaks with the free 60S fraction where precursor 60S subunits would co-migrate. In contrast, a significant fraction of 7S pre-rRNA co-migrates with polysomes in cells expressing RNA exosome mutants. The spread of 7S in polysome fractions is broader and across all polysome fractions in *rrp4-G226D* and *rrp40-W195R* cap mutant cells, compared to the 7S pre-rRNA distribution in the *rrp46-L191H* core mutant cells.

To assess whether the 7S pre-rRNA containing complexes migrating in polysome fractions in mutant strains were not aggregated complexes, we prepared cell lysates under polysome run-off conditions by removing cycloheximide and adding 2.5 mM puromycin, which dissociates the 80S ribosomes into 40S and 60S subunits. Under these conditions, a significant portion of 7S pre-rRNAs and 5.8S rRNAs was shifted to the 80S and 60S fractions in all tested strains (**Figure 6C**). These results demonstrate that bulk of the 7S pre-rRNA found in the polysome fractions of the *rrp* mutant cells was associated with ribosomes. Interestingly, the pattern of 7S pre-rRNA processing/degradation is distinct between the *rrp4-G226D, rrp40-W195R* and *rrp46-L191H* cells, further corroborating the differential molecular consequences of the RNA exosomopathy mutants.

DISCUSSION

This work represents the first *in vivo* comparative study of a collection of RNA exosomopathy mutant models. Comparison of the cellular RNAs across the modeled RNA exosomopathies in yeast provides intriguing results regarding the shared and distinctly altered transcripts and the potential pathways – metabolic and biosynthetic processes, rRNA processing/modification and ribosome biogenesis – impacted within the models analyzed. Additionally, this study revealed distinct translational defects between the *rrp4-G226D* and *rrp40-W195R* cap and *rrp46-L191H* core mutant models, including decreased global translation and quality of actively translating ribosomes. The results of this study underscore the significance of the link between consequences in RNA exosome dysfunction in exosomopathies and the molecular defects in translation efficiency and fidelity, potentially providing insight into cellular defects underlying distinct pathologies reported in exosomopathies.

Whether the molecular consequences observed in RNA exosomopathy yeast models are directly caused by changes in the integrity of the RNA exosome complex, which would affect the quantity and quality of the available RNA exosome complexes, or are due to disrupting key RNA exosome interactions with cofactors or other interacting partners, or a combination of both, remains poorly characterized. Addressing these questions will require in depth biochemical analysis of each pathogenic protein variant with regards to the impact on the complex and the exosome interactome, as the amino acid substitutions are likely to have different impacts based on the available structural information. In considering distinct consequences for the RNA exosome structure, integrity, and interactions, EXOSC2-G198D is predicted to severely impact the structural organization of the cap subunit [29, 43]. However, the pathogenic substitutions in EXOSC3 are predicted to impact interactions with surrounding subunits within the complex. The EXOSC3-D132 residue lies in a loop between strands in the S1 domain and the substitution EXOSC3-D132A likely would impair folding of the subunit and impact interactions with neighboring subunits EXOSC5 and EXOSC9 [25, 41]. Similarly, the EXOSC3-W238 residue is predicted to position other EXOSC3 residues to interact with neighboring EXOSC9 residues, thus a substitution at this position could weaken EXOSC3•EXOSC9 interactions [25, 41]. The EXOSC5 pathogenic substitutions have been predicted to have destabilizing impacts on the subunit itself and complex interactions [33]. The EXOSC5-T114 residue interacts with A62 in the N-terminal region of the subunit and the EXOSC5-T114I substitution will likely disrupt this intra-subunit interaction [33]. The EXOSC5-M148 residue is at the interface with EXOSC3 and a substitution to threonine likely will affect interactions between the subunits. The EXSOC5-L206 residue is buried in a hydrophobic pocket of the subunit. Therefore, the substitution EXOSC5-L206H is predicted to exert destabilizing effects on the integrity of the subunit [33]. Lastly, the EXOSC9-L14 residue is located in the first alpha helix of EXOSC9 and the substitution EXOSC9-L14P may disrupt interactions within the subunit [71]. In summary, the pathogenic amino acid substitutions are predicted to have varied biochemical structural consequences. As such, each RNA exosomopathy protein variant may have differential impacts on the overall structure and function of the RNA exosome complex that requires further investigation.

In growth assays, the SHRF-linked *EXOSC2-G198D* (*rrp4-G226D*), PCH-linked *EXOSC3-W238R* (*rrp40-W195R*) and cerebellar atrophy-linked *EXOSC5-L206H* (*rrp46-L191H*) mutations show the most profound growth consequences when modeled in budding yeast. These results are intriguing as the associated RNA exosomopathy disease pathologies linked to each mutation modeled in *S. cerevisiae* are diverse in the tissues impacted and the severity. The SHRF clinical outcome is relatively mild compared to the cerebellar atrophy symptoms associated with the *EXOSC5* mutations, and yet the *rrp4-G226D* mutant models show the most severe growth defect. The *EXOSC3-W238R* mutation nor the *EXOSC2-G198D* mutation has been found in the homozygous state, suggesting these mutations are lethal or highly deleterious in humans and cannot support life [26, 29, 30, 32, 38, 48]. In contrast, the *EXOSC5-L206H* mutation has been found in the homozygous state within patients [33]. While our *rrp* mutant models all show defects, the modeled *rrp4-G226D, rrp40-W195R* and *rrp46-L191H* alleles are able to support growth when expressed as the sole copy of the essential *RRP* gene. These results may suggest potential different organismal requirements for the RNA exosome activity between yeast and humans.

Differential expression analysis reveals a significant decrease in several transcripts that encode various Heat shock protein (HSP) family members in the *rrp4-G226D* cells. The significant decrease in *HSP* mRNAs could suggest that the *rrp4-G226D* cells have compromised response to heat stress, thus explaining the significant growth defect observed at 37°C. Previous work has shown that a loss of Rrp6 leads to decreased levels of *HSP* transcripts in a manner independent from the interaction between the exonuclease and the RNA exosome complex [72]. Possibly, the Rrp4-G226D variant could impact this moonlighting role of Rrp6 *in vivo*. This compromised response to stress may also explain the increase in *DDR2* and *PIR3* mRNA transcripts observed in the *rrp4-G226D* cells as expression of both these genes is activated in response to a variety of stressful conditions [84, 85]. Furthermore, the decrease in several biosynthetic transcripts observed in all three *rrp* mutants could also reflect overall slowed growth within the mutant models. These changes to conserved metabolic and biosynthetic pathways observed in the *rrp* mutants could also underlie disease pathologies in individuals with RNA exosomopathies. Among the increased transcripts observed in differential expression analysis of the three *rrp* mutant models, some

had identifiable human homologs. GO analysis of the evolutionarily conserved transcripts revealed a significant enrichment in synaptic vesicle priming and fusion biological processes. The link between these modeled RNA exosomopathy mutations and biological processes involved in synaptic vesicle fusion and trafficking may provide context for the numerous neurological defects that are common in RNA exosomopathy patients.

All three *rrp* mutant models also show a significant decrease in mRNAs that encode components of the ribosome and gene ontology analysis of shared dysregulated transcripts reveals pathways related to ribosome biogenesis and translation to be significantly enriched, pointing to potential changes in ribosome levels and/or function. In line with this, northern blots show a decrease in mature rRNA levels in *rrp4-G226D*, *rrp40-W195R* and *rrp46-L191H* yeast cells. Depletion of individual RNA exosome subunits was previously shown to inhibit pre-rRNA cleavage even at steps not directly involving the action of the RNA exosome, resulting in rRNA processing defects and reduction of mature rRNAs [73]. Indeed, besides involvement in 60S ribosome subunit maturation [74], the nuclear RNA exosome stably associates with the late 90S pre-ribosomes during their transition to pre-40S and is required for remodeling of the 90S and maturation of pre-40S subunits [75]. Our data corroborate the significant effect of RNA exosome mutants on ribosome biogenesis and further show that the effects of variations in specific subunits of the RNA exosome in exosomopathies on translation goes beyond impacting solely the defined function of the RNA exosome complex in pre-rRNA processing. Some of these effects could be caused by accumulation or reduction of levels of transcripts that are important for ribosome assembly including the snoRNAs and the specific mRNA transcripts coding for ribosomal proteins or ribosome assembly factors. Other effects could be direct or indirect due to reduced or incomplete processing of the precursor rRNAs. Impaired processing of rRNA could result in assembly of dysfunctional ribosomes that are either quality controlled and discarded causing reduced ribosome numbers or escape into the translating pool of ribosomes, e.g., those containing 7S pre-rRNAs.

Maturation of the 3′ end the 5.8S rRNA from the 7S pre-rRNAs involves a series of cleavages by different nucleases [74]. The trimming of 7S to 6S pre-rRNA happens in the nucleus whereas the final processing of 6S pre-rRNA to 5.8S rRNA is cytoplasmic [76]. However, immature 60S ribosome subunits

containing the variants of 7S pre-rRNA have been previously reported to escape the nucleus and engage in translation in mutant yeast. In mutant *rrp6Δ* yeast, pre-60S ribosomes containing nuclear 5.8S rRNA and an additional 30 nucleotides of the ITS2 region were shown to escape to the cytoplasm and enter the polysome pool [50]. Similarly, expression of a variant of the RNA exosome cofactor Mtr4 helicase was reported to result in accumulation of nuclear pre-60S ribosomes containing 7S pre-rRNA in the cytoplasm [70]. These premature ribosomes were shown to engage in translation suggesting 7S pre-rRNA processing defects do not prevent the export of 7S-containing pre-60S ribosomes [70]. In the context of 40S maturation, the trimming of the 3'-end of 18S rRNA from its precursor 20S pre-rRNA also occurs in the cytoplasm and requires the endonuclease Nob1 [77-80]. This step is strictly quality controlled by a kinase-dependent check point that prevents entry of premature 20S-containing 40S ribosomal subunits into translating pool of ribosomes [81]. However, cytoplasmic pre-40S ribosomes escape into the translating pool in several mutant yeast strains that fail the surveillance pathways during 40S assembly [81-85]. Our data indicate that the cap vs core RNA exosome subunit variants cause distinct translational defects, with mutant cap variants Rrp4-G226D and Rrp40-W195R showing a formation of halfmers and indicating a potential problem in 60S maturation or subunit joining, while the core Rrp46-L191H variant leads to a simple reduction of ribosomes. Our results suggest that the bulk of 7S pre-rRNA ribosomes enter the translation pool, albeit not as efficiently as 5.8S-containing ribosome, in the cap mutant strains compared to the core mutant strains. Future mechanistic studies are needed to dissect how a shortage of healthy ribosomes and the presence of 7S-containing ribosomes in the translation pool impact the cellular proteome in these RNA exosomopathy models. Overall, variation in both the cap and core RNA exosome subunits could significantly change the translating ribosome pool and cellular proteome. However, the cap and core mutants appear to impact translation in distinct ways, likely due to the different rRNA intermediates, contributing to the unique molecular consequences and pathologies in each modeled disease. Importantly, of the two cap subunit variants modeled, the *rrp4-G226D* mutation causes a severe growth defect at 30˚C whereas the *rrp40-W195R* shows a slight growth defect. Thus, global shortage of ribosomes and RNA exosome cannot simply explain the severity of the molecular impact from each mutant and the overall growth fitness. Therefore, even though the

simplest way to interpret the severity of RNA exosomopathy mutants may be an RNA exosome concentration drop model which would affect transcript levels, the molecular pathology of RNA exosomopathy mutants appears far more complex and likely impacted by transcriptional, post-transcriptional and translational mechanisms that require further investigation.

In summary, data presented in this study provide novel insights into molecular mechanisms of defects caused by RNA exosomopathy-linked mutants in yeast models and reveal that different RNA exosomopathy mutations result in both unique and shared molecular changes across variants. Our data suggest that while RNA exosomopathies are a conglomeration of many direct and indirect molecular changes at the transcript level, translational defects that affect protein homeostasis and cellular outcomes likely contribute to the distinct cellular outcomes from the RNA exosomopathy-causing mutations. Thus, even though distinct in their sources, RNA exosomopathies share phenotypic and mechanistic similarities among themselves and with ribosomopathies. Future work is required to reveal why despite affecting molecular mechanisms that are seemingly universal to all cells, neuronal cells are most affected by these groups of diseases. Likely changes in the transcript levels, ribosome numbers, quality, and fidelity of translation in RNA exosomopathies alter the translation of specific mRNAs involved in neuronal differentiation and/or function to cause tissue-specific molecular defects.

MATERIALS AND METHODS

Saccharomyces cerevisiae strains and plasmids. S. cerevisiae strains and plasmids used in this study are listed in **Table S2**. Oligonucleotides used for plasmid construction are listed in **Table S3**. The *rrp4*Δ (yAV1103), *rrp40*Δ (yAV1107), and *rrp46*Δ (yAV1105) strains used in this study were previously described [33, 86]. The *rrp45*Δ (yAV1410) strain used in this study was obtained by transforming a *RRP45 URA3* plasmid into the heterozygous diploid *RRP45/rrp45*Δ strain from the knock out collection and sporulating the transformants to obtain a haploid *rrp45*Δ strain. The *rrp6*Δ strain (ACY1641) was obtained from Horizon Discovery. The wild-type *RRP4* (pAC3656), *RRP40* (pAC3652), and *RRP46* (pAC3482) plasmids were constructed as previously described and each contain the open reading frame (ORF) flanked by endogenous regulatory sequences (promoter, terminator and 5'/3' UTR) cloned into the

pRS315 vector (ATTC #77144), which harbors the *LEU2* marker [33, 41, 43]. The wild-type *RRP45* (pAV975) plasmid contains the ORF flanked by endogenous regulatory sequences cloned into the pRS415 *LEU2* vector. The *rrp4-G226D* (pAC3659), *rrp40-S87A* (pAC3654), *rrp40-W195R* (pAC3655), *rrp46-Q86I* (pAC3483), *rrp46-L127T* (pAC3534), and *rrp46-L191H* (pAC3484) mutant plasmids encoding the different RNA exosomopathy amino acid substitutions were generated by site-directed mutagenesis of the respective wild-type plasmids (pAC3656, pAC3652, pAC3482) using the QuikChange II Site-Directed Mutagenesis Kit (Agilent) and oligonucleotides containing the desired missense mutations as previously described [33, 41, 43]. The *rrp45-I15P* (pAC3480) mutant plasmid was generated by site-directed mutagenesis of pAV975 using oligonucleotides AC8001 and AC8002 in this study. The wild-type *RRP6* (pAC3752) plasmid was constructed by subcloning ApaI/SacI-digested *RRP6* ORF with endogenous regulatory sequences from pAC2301 (*RRP6* in pRS313; Fasken et al. PLOS Genetics (2015)) into pRS315 cut with ApaI/SacI. The *TEF1p-Cas9-CYC1t-SNR52p* (pAC3846) pCas9 plasmid was constructed by PCR amplification of *TEF1p* with oligonucleotides AC8410 and AC8411 and *Cas9-CYC1t* with AC6802 and AC6803 using p414-*TEF1p-Cas9-CYC1t* plasmid template (Addgene #43802, [87]) and *SNR52p* with AC6804 and AC6805 using p426-SNR52p-gRNA.CAN1.Y-SUP4t plasmid template (Addgene #43803, [87]), followed by sequential cloning of SacI/SpeI-digested *TEF1p*, SpeI/KpnI-digested *Cas9-CYC1t*, and AgeI/KpnI-digested *SNR52p* into pRS316 plasmid digested with corresponding restriction enzymes. The *TEF1p-Cas9-CYC1t-SNR52p-RRP4_668.gRNA-SUP4t* (pAC3863), *TEF1p-Cas9-CYC1t-SNR52p-RRP40_583.gRNA-SUP4t* (pAC3861), and *TEF1p-Cas9-CYC1t-SNR52p-RRP46_589.gRNA-SUP4t* (pAC4342) pCas9 plasmids containing the gRNAs for targeting *RRP4*, *RRP40*, and *RRP46*, respectively, were constructed by PCR amplification of *RRP4_668.gRNA* with oligonucleotides AC8407 and AC6809, *RRP40_583.gRNA* with AC8402 and AC6809, and *RRP46_589.gRNA* with AC9888 and AC6809 using p426-SNR52p-gRNA.CAN1.Y-SUP4t plasmid template (Addgene #43803) and cloning of SphI/KpnI-digested gRNA products into pAC3846 digested with SphI/KpnI. All plasmids were fully sequenced.

Generation of S. cerevisiae mutant strains using *CRISPR-Cas9 genome editing*. The *rrp4-G226D* (ACY3110), *rrp40-W195R* (ACY3117), and *rrp46-L191H* (ACY3137) mutant strains were generated using CRISPR/Cas9 editing with a single pCas9-gRNA expression plasmid and double-stranded homology-directed repair (HDR) oligonucleotides in a wild-type BY4741 strain essentially as described before [87]. The single pCas9-gRNA plasmid on a pRS316 (*URA3, CEN6*) backbone is derived from p414-*TEF1p-Cas9-CYC1t* plasmid (Addgene #43802) and p426-SNR52p-gRNA.CAN1.Y-SUP4t plasmid (Addgene #43803). Constitutive expression of Cas9 is driven by the *TEF1* promoter and constitutive expression of the gRNA is driven by the *SNR52* promoter. Specifically, 500 ng of pAC3846 (pCas9 without gRNA), pAC3863 (pCas9 + *RRP4* gRNA) +/- 1 nmol of double-stranded *rrp4-G226D* HDR oligonucleotide (AC8408/8409), pAC3861 (pCas9 + *RRP40* gRNA) +/- 1 nmol double-stranded *rrp40-W195R* HDR oligonucleotide (AC8404/8405), or pAC4342 (pCas9 + *RRP46* gRNA) +/- 1 nmol double-stranded *rrp46-L191H* HDR oligonucleotide (AC9889/9890) and 50 µg salmon sperm DNA was transformed into wild-type BY4741 cells by standard Lithium Acetate (LiOAc) transformation protocol [88]. HDR oligonucleotides are listed in **Table S3**. Cells were plated on SD -Ura media plates and incubated at 30°C for 2 days. Large colonies on plates with cells transformed pCas9-gRNA and HDR oligonucleotides were restreaked to new SD -Ura media plates and screened for the presence of *rrp4-G226D*, *rrp40-W195R*, and *rrp46-L191H* mutations via Sanger sequencing of genomic *RRP4*, *RRP40*, and *RRP46* PCR products, respectively.

S. cerevisiae transformations and growth assays. All yeast transformations were performed using the standard Lithium Acetate (LiOAc) protocol [88]. Standard plasmid shuffle assays were performed to assess the *in vivo* function of the *rrp* variants as previously described [33, 41, 43]. The *rrp*Δ cells (*rrp4*Δ (yAV1103), *rrp40*Δ (yAV1107), *rrp45*Δ (yAV1410), *rrp46*Δ (yAV1105)) transformed with the wild-type control *LEU2* plasmid (*RRP4* (pAC3656), *RRP40* (pAC3652), *RRP45* (pAV975), *RRP46* (pAC3482)) or the mutant variant plasmid (*rrp4-G226D* (pAC3659), *rrp40-S87A* (pAC3654), *rrp40-W195R* (pAC3655), *rrp45-I15P* (pAC3480), *rrp46-Q86I* (pAC3483), *rrp46-L127T* (pAC3534), *rrp46-L191H* (pAC3484)) were streaked on 5-FOA SD -Leu media plates and incubated at 30°C for 2-3 days. Single colonies from the

5-FOA SD -Leu media plates were selected in quadruplicate and streaked onto selective SD -Leu media plates. The *rrp6*Δ cells (ACY1641) were transformed with empty *LEU2* vector (pRS315) or wild-type *LEU2* plasmid (*RRP6* (pAC3752)) and selected on SD -Leu media plates. The *rrp*Δ cells containing only the wild-type *RRP* or mutant *rrp LEU2* plasmid were used for the RNA-seq analysis, northern blots, and reporter assays. The CRISPR/Cas9-edited *rrp4-G226D* (ACY3110), *rrp40-W195R* (ACY3117), and *rrp46-L191H* (ACY3137) mutant cells were assessed for temperature-sensitive (ts) growth by a solid media growth assay and rescue of the ts growth of the mutant cells by wild-type *RRP4*, *RRP40*, and *RRP46* plasmids was confirmed. The *rrp4-G226D*, *rrp40-W195R*, and *rrp46-L191H* CRISPR mutant cells were used for the HPG incorporation experiment and the polysome profiling assay. Growth assays were performed on solid media and in liquid culture. The wild-type control cells and the mutant model cells were grown to saturation at 30°C before the concentrations were adjusted to an A_{600} ~0.5, and samples were serially diluted in 10-fold steps and spotted onto SD -Leu media plates. Plates were grown at 30°C and 37°C for 2-3 days. For growth in liquid culture, saturated overnight cultures grown at 30°C were diluted to an A_{600} ~0.01 in SD -Leu in a 24-well plate, and growth at 37°C was monitored and recorded at OD_{600} in a BioTek® SynergyMx microplate reader with Gen5™ v2.04 software over 24 hr. For each sample analyzed in growth assays at least 3 independent biological replicates were used. In addition, for the liquid culture assays, technical triplicate for each biological sample were grown. Doubling times were calculated using GraphPad Prism version 9.3.1.

Sample collection for RNA-seq analysis. RNA-seq was performed on three independent biological replicates of *rrp*Δ cells containing the *RRP* wild-type control plasmids or the *rrp* variants as the sole copy of the RNA exosome gene. The *rrp6*Δ cells (ACY1641) contained either an *RRP6* wild-type control plasmid (pAC3752) or an empty vector. Biological replicates of all samples were first screened by solid media growth assays prior to growth and collection for the RNA-seq experiment. For sample collection, cells were grown in SD -Leu media overnight at 30°C to saturation, diluted to A_{600} ~0.2 in SD -Leu media and shifted to 37°C for 5 hours. Cells were washed, pelleted and flash frozen and cell pellets were sent to Zymo Research for total RNA preparation and RNA-Seq analysis.

RNA-seq Library Preparation. RNA-seq library preparation was performed by Zymo Research. Total RNA-seq libraries were constructed from 300 ng of total RNA. To remove rRNA, a method previously described [89] was followed with some modifications. Libraries were prepared using the Zymo-Seq RiboFree Total RNA Library Prep Kit (Cat # R3000). RNA-seq libraries were sequenced on an Illumina NovaSeq to a sequencing depth of at least 20 million read pairs (150 bp paired-end sequencing) per sample.

Sequence Data Alignments and Differential Expression Analysis. NovaSeq paired-end 150-bp reads from Total RNA-seq data files were first adaptor trimmed, and then analyzed using the STAR program (version 2.6.1d) for alignment of short reads to *S. cerevisiae* reference genome. Transcript and gene expression estimates were measured using StringTie v2.1.7 [90]. The expression estimates fragments per Kilobase of transcript per Million mapped (FPKM) were used with the Pheatmap R package v1.0.12 to generate heatmaps [91]. The raw reads were per gene feature counted using featureCounts v1.22.2 [92] to the *S. cerevisiae* S288C genome assembly R64-1-1 [93], annotated with CUTs and SUTs [64]. Low feature counts (<10 reads total) were removed. Differential gene expression analysis on raw read counts was performed using the DESeq2 R package v1.38.1 [94] to identify genes significantly changed (p-value<0.05, ≥1.5-fold change) in *rrp* mutant variant samples relative to *RRP* wild-type control samples. Shrinkage of effect size was performed on differential expression data for visualizations using the *apeglm* method [95]. Using DESeq2, principal component analysis (PCA) was performed, and MA plots were generated on raw read counts. Volcano plots of differential gene expression data were produced using EnhancedVolcano R package v1.16.0 [96]. UpSet plots were generated using UpSetR R package v1.4.0 [97], with transcripts identified through differential expression analysis in the mutant cells as significantly decreased by 1.5-fold or more (FC≤-1.5) and significantly increased by 1.5-fold or more (FC≥+1.5). UpSet intersections are shown in graphs as a matrix, with rows corresponding to the sets of samples (i.e., transcripts identified FC≤-1.5 or FC≥+1.5 within the three mutant models) and columns corresponding to the intersection between these sets. Piecharts and stacked bars of RNA class

percentages in significantly altered genes were generated using GraphPad Prism version 9.3.1. Transcripts were sorted by class using the annotations available through the *Saccharomyces cerevisiae Genome Database* (SGD) [98]. Gene Ontology (GO) analysis on significantly altered genes for Biological Process category was performed using the YeastMine webserver. GO analysis on human homolog genes was performed using HumanMine. All GO analyses were performed by Holm-Bonferroni test correction. The full RNA-Seq datasets, enriched transcripts and GO analyses are compiled in Supplemental Documentations S1-S3.

Northern Blot Analysis of rRNAs. For analysis of ribosomal RNAs, yeast cells were grown to mid-log phase and RNA was extracted using the hot phenol method. Northern blotting was carried out essentially as previously described [99], using the following probes: 18S, CATGGCTTAATCTTTGAGAC; 25S, GCCCGTTCCCTTGGCTGTG; 5.8S, CTGCGTTCTTGATCGATGCG; between A3 and 5.8S, CCA GTT ACG AAA ATT CTT G.

Assay of Global Translation. To assay global changes in translation, cells were transformed with pRS411 plasmid and grown in minimal media lacking methionine to late log phase. L-Homopropargylglycine (HPG) was added to 2 mL cultures to a final concentration of 50 μM, and cells were incubated for 30 min at 30 °C. Negative controls received fresh cycloheximide at a final concentration of 0.1 mg/ml before the addition of HPG. The cell pellets were resuspended in 100 μL of lysis buffer (50 mM Tris-HCl, pH 7.4, 150 mM NaCl, 1 mM ethylenediamine tetraacetic acid (EDTA), 1 mM ethylene glycol tetraacetic acid (EGTA), 1% Triton X-100, 1% sodium deoxycholate, and 0.1% SDS) supplemented with protease inhibitors, mixed with disruption beads, and lysed in a bead beater. After clearing the lysate, the protein concentration was measured by bicinchoninic acid (BCA) (Thermo Fisher), and an equal amount of protein was used for labeling by Alexa Fluor 488 using the Click-iT HPG Alexa Fluor 488 protein synthesis assay kit (Thermo Fisher). Labeled nascent proteins were resolved on a 12% SDS gel and visualized on a ChemiDoc Imager (Bio-Rad). Total protein was visualized after Coomassie staining and imaged using ChemiDoc.

Dual-Luciferase Reporter Assays to Monitor Translation Fidelity Defects. For assaying translation fidelity defects, cells expressing wild-type or variant RNA exosome subunits and a dual-luciferase reporter plasmid were grown to mid-log phase in Ura$^-$, Leu$^-$ synthetic glucose liquid media. Cells were pelleted, washed, and stored at −80 °C before analysis. Luciferase activities were measured using the Dual-Luciferase Reporter Assay kit (Promega). Thawed frozen cell pellets were resuspended in 1 X Passive Lysis Buffer and incubated for 10 min. LARII was mixed with lysate in clear bottom 96-well Microplates (Costar), and Firefly luciferase activity was measured. Stop and Glo solution was added, and Renilla luciferase activity was measured. Measurements were performed using a Synergy Microplate reader (BioTek). For each biological replicate (single transformant), the Firefly luciferase signal was normalized to the Renilla luciferase signal. For each strain, Firefly/Renilla ratio was normalized to the average Firefly/Renilla ratio of replicates containing a control plasmid.

Sucrose density gradient analysis. For analysis of polysomes by gradients, cells were grown to mid-log phase in YP-dextrose media at 37˚C and harvested after addition of 0.1 mg/ml cycloheximide or no cycloheximide. Cells were washed and lysed in ice-cold gradient buffer (20 mM HEPES, pH 7.4, 5 mM $MgCl_2$, 100 mM NaCl, and 2 mM DTT) supplemented with complete protease Inhibitor cocktail (Roche) and 0.1 mg/ml cycloheximide or no cycloheximide. Cells were broken by cryogenic grinding and cell lysate was cleared by centrifugation at 10,000 g for 10 min. The absorbance of cleared lysate was measured at UV_{260} and equal amount of lysate was applied to 10–50% sucrose gradients in gradient buffer for all samples. To samples lacking cycloheximide, 2.5 mM puromycin was added to the cleared cell lysate and incubated on ice for 15 min and then placed at 37˚C before loading onto the gradient. Gradients were centrifuged for 2 h at 40,000 RPM in a SW41Ti rotor and fractionated using a BioComp fraction collector.

ACKNOWLEDGEMENTS

We thank members of the Corbett and Ghalei laboratories for critical discussions and input. We thank Dr. Benjamin Barwick for his contributions in assisting with the analysis of the CoMMpass dataset. This work

was supported by NIH awards R35GM138123 to H.G., R35GM141710 to AvH, and R01GM130147 to AvH and AHC, as well as funds from a Synergy II Nexus Award provided by the Woodruff Health Sciences Center (WHSC), Emory School of Medicine, the Office of the Provost, and Emory College of Arts and Sciences (ECAS) to H.G. and A.H.C. M.C.S. was supported by an F31 grant from the National Institutes of Health. L.A.C. was supported by NIH T32GM149422.

REFERENCES

1. Corbett, A.H., *Post-transcriptional regulation of gene expression and human disease.* Curr Opin Cell Biol, 2018. **52**: p. 96-104.
2. Makino, D.L., M. Baumgaertner, and E. Conti, *Crystal structure of an RNA-bound 11-subunit eukaryotic exosome complex.* Nature, 2013. **495**(7439): p. 70-75.
3. Mitchell, P., et al., *The exosome: A conserved eukaryotic RNA processing complex containing multiple 3'->5' exoribonucleases.* Cell, 1997. **91**(4): p. 457-466.
4. Mitchell, P., E. Petfalski, and D. Tollervey, *The 3' end of yeast 5.8S rRNA is generated by an exonuclease processing mechanism.* Genes Dev, 1996. **10**(4): p. 502-13.
5. Bonneau, F., et al., *The yeast exosome functions as a macromolecular cage to channel RNA substrates for degradation.* Cell, 2009. **139**(3): p. 547-59.
6. Liu, Q., J.C. Greimann, and C.D. Lima, *Reconstitution, activities, and structure of the eukaryotic RNA exosome.* Cell, 2006. **127**(6): p. 1223-1237.
7. Wasmuth, E.V., K. Januszyk, and C.D. Lima, *Structure of an Rrp6-RNA exosome complex bound to poly(A) RNA.* Nature, 2014. **511**(7510): p. 435-9.
8. Zinder, J.C., E.V. Wasmuth, and C.D. Lima, *Nuclear RNA Exosome at 3.1 A Reveals Substrate Specificities, RNA Paths, and Allosteric Inhibition of Rrp44/Dis3.* Mol Cell, 2016. **64**(4): p. 734-745.
9. Kilchert, C., S. Wittmann, and L. Vasiljeva, *The regulation and functions of the nuclear RNA exosome complex.* Nature Reviews Molecular Cell Biology, 2016. **17**(4): p. 227-239.
10. Morton, D.J., et al., *The RNA exosome and RNA exosome-linked disease.* Rna, 2018. **24**(2): p. 127-142.
11. Schneider, C. and D. Tollervey, *Threading the barrel of the RNA exosome.* Trends in Biochemical Sciences, 2013. **38**(10): p. 485-493.
12. Chekanova, J.A., et al., *Genome-wide high-resolution mapping of exosome substrates reveals hidden features in the Arabidopsis transcriptome.* Cell, 2007. **131**(7): p. 1340-53.
13. Gudipati, R.K., et al., *Extensive degradation of RNA precursors by the exosome in wild-type cells.* Mol Cell, 2012. **48**(3): p. 409-21.
14. Schneider, C., et al., *Transcriptome-wide Analysis of Exosome Targets.* Molecular Cell, 2012. **48**(3): p. 422-433.
15. Pefanis, E., et al., *Noncoding RNA transcription targets AID to divergently transcribed loci in B cells.* Nature, 2014. **514**(7522): p. 389-93.
16. Allmang, C., et al., *Functions of the exosome in rRNA, snoRNA and snRNA synthesis.* Embo Journal, 1999. **18**(19): p. 5399-5410.
17. Parker, R., *RNA Degradation in Saccharomyces cerevisae.* Genetics, 2012. **191**(3): p. 671-702.
18. Wyers, F., et al., *Cryptic Pol II Transcripts Are Degraded by a Nuclear Quality Control Pathway Involving a New Poly(A) Polymerase.* Cell, 2005. **121**(5): p. 725-737.
19. Kiss, D.L. and E.D. Andrulis, *Genome-wide analysis reveals distinct substrate specificities of Rrp6, Dis3, and core exosome subunits.* Rna, 2010. **16**(4): p. 781-791.
20. Belair, C., S. Sim, and S.L. Wolin, *Noncoding RNA Surveillance: The Ends Justify the Means.* Chemical Reviews, 2018. **118**(8): p. 4422-4447.
21. Molleston, J.M., et al., *A conserved virus-induced cytoplasmic TRAMP-like complex recruits the exosome to target viral RNA for degradation.* Genes & Development, 2016. **30**(14): p. 1658-1670.
22. Hou, D., M. Ruiz, and E.D. Andrulis, *The ribonuclease Dis3 is an essential regulator of the developmental transcriptome.* Bmc Genomics, 2012. **13**.
23. Lim, S.J., et al., *Genome-wide localization of exosome components to active promoters and chromatin insulators in Drosophila.* Nucleic Acids Res, 2013. **41**(5): p. 2963-80.
24. Lorentzen, E., et al., *RNA channelling by the archaeal exosome.* Embo Reports, 2007. **8**(5): p. 470-476.

25. Fasken, M.B., et al., *The RNA Exosome and Human Disease.* Methods Mol Biol, 2020. **2062**: p. 3-33.
26. Biancheri, R., et al., *EXOSC3 mutations in isolated cerebellar hypoplasia and spinal anterior horn involvement.* J Neurol, 2013. **260**(7): p. 1866-70.
27. Boczonadi, V., et al., *EXOSC8 mutations alter mRNA metabolism and cause hypomyelination with spinal muscular atrophy and cerebellar hypoplasia.* Nature Communications, 2014. **5**.
28. Burns, D.T., et al., *Variants in EXOSC9 Disrupt the RNA Exosome and Result in Cerebellar Atrophy with Spinal Motor Neuronopathy.* Am J Hum Genet, 2018. **102**(5): p. 858-873.
29. Di Donato, N., et al., *Mutations in EXOSC2 are associated with a novel syndrome characterised by retinitis pigmentosa, progressive hearing loss, premature ageing, short stature, mild intellectual disability and distinctive gestalt.* Journal of Medical Genetics, 2016. **53**(6): p. 419-425.
30. Eggens, V.R.C., et al., *EXOSC3 mutations in pontocerebellar hypoplasia type 1: novel mutations and genotype-phenotype correlations.* Orphanet Journal of Rare Diseases, 2014. **9**(1): p. 23.
31. Schottmann, G., et al., *Recessive mutation in EXOSC3 associates with mitochondrial dysfunction and pontocerebellar hypoplasia*. Vol. 37. 2017.
32. Wan, J., et al., *Mutations in the RNA exosome component gene EXOSC3 cause pontocerebellar hypoplasia and spinal motor neuron degeneration.* Nature Genetics, 2012. **44**(6): p. 704-U134.
33. Slavotinek, A., et al., *Biallelic variants in the RNA exosome gene EXOSC5 are associated with developmental delays, short stature, cerebellar hypoplasia and motor weakness.* Hum Mol Genet, 2020. **29**(13): p. 2218-2239.
34. Somashekar, P.H., et al., *Bi-allelic missense variant, p.Ser35Leu in EXOSC1 is associated with pontocerebellar hypoplasia.* Clin Genet, 2021. **99**(4): p. 594-600.
35. Wan, J., et al., *Mutations in the RNA exosome component gene EXOSC3 cause pontocerebellar hypoplasia and spinal motor neuron degeneration.* Nat Genet, 2012. **44**(6): p. 704-8.
36. Bizzari, S., et al., *Expanded PCH1D phenotype linked to EXOSC9 mutation.* Eur J Med Genet, 2020. **63**(1): p. 103622.
37. Burns, D., et al., *A recessive mutation in EXOSC9 causes abnormal RNA metabolism resulting in a novel form of cerebellar hypoplasia/atrophy with early motor neuronopathy.* Neuromuscul Disord, 2017. **27**: p. S38.
38. Halevy, A., et al., *Novel EXOSC3 mutation causes complicated hereditary spastic paraplegia.* J Neurol, 2014. **261**(11): p. 2165-9.
39. Sakamoto, M., et al., *Novel EXOSC9 variants cause pontocerebellar hypoplasia type 1D with spinal motor neuronopathy and cerebellar atrophy.* J Hum Genet, 2021. **66**(4): p. 401-407.
40. Damseh, N.S., et al., *Pontocerebellar hypoplasia associated with p.Arg183Trp homozygous variant in EXOSC1 gene: A case report.* Am J Med Genet A, 2023. **191**(7): p. 1923-1928.
41. Fasken, M.B., et al., *Insight into the RNA Exosome Complex Through Modeling Pontocerebellar Hypoplasia Type 1b Disease Mutations in Yeast.* Genetics, 2017. **205**(1): p. 221-+.
42. Gillespie, A., et al., *Mutations of EXOSC3/Rrp40p associated with neurological diseases impact ribosomal RNA processing functions of the exosome in S. cerevisiae.* RNA, 2017. **23**(4): p. 466-472.
43. Sterrett, M.C., et al., *A budding yeast model for human disease mutations in the EXOSC2 cap subunit of the RNA exosome complex.* RNA, 2021. **27**(9): p. 1046-1067.
44. Morton, D.J., B., Jalloh, I., Kremsky, L., Kim, T., Le, K., Nguyen, J.C., Rounds, M.C., Sterrett, B., Brown, S.W., Leung, M.B., Fasken, K.H., Moberg, A.H., Corbett, *A Drosophila Model of Pontocerebellar Hypoplasia Reveals a Critical Role for the RNA Exosome in Neurons.* BioRxiv 727693 2019. **[Preprint]**
45. Mitchell, P., et al., *The exosome: a conserved eukaryotic RNA processing complex containing multiple 3'-->5' exoribonucleases.* Cell, 1997. **91**(4): p. 457-66.
46. Belair, C., et al., *The RNA exosome nuclease complex regulates human embryonic stem cell differentiation.* J Cell Biol, 2019.

47. Wasmuth, E.V., et al., *Structure and reconstitution of yeast Mpp6-nuclear exosome complexes reveals that Mpp6 stimulates RNA decay and recruits the Mtr4 helicase.* Elife, 2017. **6**: p. 24.
48. Rudnik-Schoneborn, S., et al., *Pontocerebellar hypoplasia type 1: clinical spectrum and relevance of EXOSC3 mutations.* Neurology, 2013. **80**(5): p. 438-46.
49. Wan, J., et al., *Mutations in the RNA exosome component gene EXOSC3 cause pontocerebellar hypoplasia and spinal motor neuron degeneration.* Nature genetics, 2012. **44**(6): p. 704-8.
50. Briggs, M.W., K.T. Burkard, and J.S. Butler, *Rrp6p, the yeast homologue of the human PM-Scl 100-kDa autoantigen, is essential for efficient 5.8 S rRNA 3' end formation.* J Biol Chem, 1998. **273**(21): p. 13255-63.
51. Marin-Vicente, C., et al., *RRP6/EXOSC10 is required for the repair of DNA double-strand breaks by homologous recombination.* Journal of Cell Science, 2015. **128**(6): p. 1097-1107.
52. Schuch, B., et al., *The exosome-binding factors Rrp6 and Rrp47 form a composite surface for recruiting the Mtr4 helicase.* Embo Journal, 2014. **33**(23): p. 2829-2846.
53. Fasken, M.B., et al., *Insight into the RNA Exosome Complex Through Modeling Pontocerebellar Hypoplasia Type 1b Disease Mutations in Yeast.* Genetics, 2017. **205**(1): p. 221-237.
54. Bush, G.L. and D.I. Meyer, *The refolding activity of the yeast heat shock proteins Ssa1 and Ssa2 defines their role in protein translocation.* J Cell Biol, 1996. **135**(5): p. 1229-37.
55. Unno, K., et al., *Role of Hsp70 subfamily, Ssa, in protein folding in yeast cells, seen in luciferase-transformed ssa mutants.* Biol Pharm Bull, 1997. **20**(12): p. 1240-4.
56. López-Ribot, J.L. and W.L. Chaffin, *Members of the Hsp70 family of proteins in the cell wall of Saccharomyces cerevisiae.* J Bacteriol, 1996. **178**(15): p. 4724-6.
57. Brown, C.R., J.A. McCann, and H.L. Chiang, *The heat shock protein Ssa2p is required for import of fructose-1, 6-bisphosphatase into Vid vesicles.* J Cell Biol, 2000. **150**(1): p. 65-76.
58. Borkovich, K.A., et al., *hsp82 is an essential protein that is required in higher concentrations for growth of cells at higher temperatures.* Mol Cell Biol, 1989. **9**(9): p. 3919-30.
59. Gross, D.S., et al., *Promoter function and in situ protein/DNA interactions upstream of the yeast HSP90 heat shock genes.* Antonie Van Leeuwenhoek, 1990. **58**(3): p. 175-86.
60. Planta, R.J. and W.H. Mager, *The list of cytoplasmic ribosomal proteins of Saccharomyces cerevisiae.* Yeast, 1998. **14**(5): p. 471-7.
61. Davis, C.A. and M. Ares, Jr., *Accumulation of unstable promoter-associated transcripts upon loss of the nuclear exosome subunit Rrp6p in Saccharomyces cerevisiae.* Proc Natl Acad Sci U S A, 2006. **103**(9): p. 3262-7.
62. Gudipati, R.K., et al., *Extensive Degradation of RNA Precursors by the Exosome in Wild-Type Cells.* Molecular Cell, 2012. **48**(3): p. 409-421.
63. Wyers, F., et al., *Cryptic Pol II transcripts are degraded by a nuclear quality control pathway involving a new poly(A) polymerase.* Cell, 2005. **121**(5): p. 725-737.
64. Xu, Z., et al., *Bidirectional promoters generate pervasive transcription in yeast.* Nature, 2009. **457**(7232): p. 1033-7.
65. Fox, M.J., et al., *The Exosome Component Rrp6 Is Required for RNA Polymerase II Termination at Specific Targets of the Nrd1-Nab3 Pathway.* PLOS Genetics, 2015. **11**(2): p. e1004999.
66. Harger, J.W. and J.D. Dinman, *An in vivo dual-luciferase assay system for studying translational recoding in the yeast Saccharomyces cerevisiae.* RNA, 2003. **9**(8): p. 1019-24.
67. Cheung, Y.N., et al., *Dissociation of eIF1 from the 40S ribosomal subunit is a key step in start codon selection in vivo.* Genes Dev, 2007. **21**(10): p. 1217-30.
68. Salas-Marco, J. and D.M. Bedwell, *Discrimination between defects in elongation fidelity and termination efficiency provides mechanistic insights into translational readthrough.* J Mol Biol, 2005. **348**(4): p. 801-15.
69. Plant, E.P., et al., *Differentiating between near- and non-cognate codons in Saccharomyces cerevisiae.* PLoS One, 2007. **2**(6): p. e517.

70. Rodríguez-Galán, O., et al., *Immature large ribosomal subunits containing the 7S pre-rRNA can engage in translation in Saccharomyces cerevisiae.* RNA Biol, 2015. **12**(8): p. 838-46.
71. Liu, J.J., et al., *CryoEM structure of yeast cytoplasmic exosome complex.* Cell Res, 2016. **26**(7): p. 822-37.
72. Wang, C., et al., *Rrp6 Moonlights in an RNA Exosome-Independent Manner to Promote Cell Survival and Gene Expression during Stress.* Cell Reports, 2020. **31**(10): p. 107754.
73. Allmang, C., et al., *Degradation of ribosomal RNA precursors by the exosome.* Nucleic Acids Res, 2000. **28**(8): p. 1684-91.
74. Fernández-Pevida, A., D. Kressler, and J. de la Cruz, *Processing of preribosomal RNA in Saccharomyces cerevisiae.* Wiley Interdiscip Rev RNA, 2015. **6**(2): p. 191-209.
75. Lau, B., et al., *Structure of the Maturing 90S Pre-ribosome in Association with the RNA Exosome.* Mol Cell, 2021. **81**(2): p. 293-303.e4.
76. Thomson, E. and D. Tollervey, *The final step in 5.8S rRNA processing is cytoplasmic in Saccharomyces cerevisiae.* Mol Cell Biol, 2010. **30**(4): p. 976-84.
77. Fatica, A., et al., *Nob1p is required for cleavage of the 3' end of 18S rRNA.* Mol Cell Biol, 2003. **23**(5): p. 1798-807.
78. Fatica, A., D. Tollervey, and M. Dlakić, *PIN domain of Nob1p is required for D-site cleavage in 20S pre-rRNA.* Rna, 2004. **10**(11): p. 1698-701.
79. Lamanna, A.C. and K. Karbstein, *Nob1 binds the single-stranded cleavage site D at the 3'-end of 18S rRNA with its PIN domain.* Proc Natl Acad Sci U S A, 2009. **106**(34): p. 14259-64.
80. Pertschy, B., et al., *RNA helicase Prp43 and its co-factor Pfa1 promote 20 to 18 S rRNA processing catalyzed by the endonuclease Nob1.* J Biol Chem, 2009. **284**(50): p. 35079-91.
81. Parker, M.D., et al., *A kinase-dependent checkpoint prevents escape of immature ribosomes into the translating pool.* PLoS Biol, 2019. **17**(12): p. e3000329.
82. Parker, M.D. and K. Karbstein, *Quality control ensures fidelity in ribosome assembly and cellular health.* J Cell Biol, 2023. **222**(4).
83. Soudet, J., et al., *Immature small ribosomal subunits can engage in translation initiation in Saccharomyces cerevisiae.* Embo j, 2010. **29**(1): p. 80-92.
84. Strunk, B.S., et al., *A translation-like cycle is a quality control checkpoint for maturing 40S ribosome subunits.* Cell, 2012. **150**(1): p. 111-21.
85. García-Gómez, J.J., et al., *Final pre-40S maturation depends on the functional integrity of the 60S subunit ribosomal protein L3.* PLoS Genet, 2014. **10**(3): p. e1004205.
86. Schaeffer, D., et al., *The exosome contains domains with specific endoribonuclease, exoribonuclease and cytoplasmic mRNA decay activities.* Nat Struct Mol Biol, 2009. **16**(1): p. 56-62.
87. DiCarlo, J.E., et al., *Genome engineering in Saccharomyces cerevisiae using CRISPR-Cas systems.* Nucleic Acids Res, 2013. **41**(7): p. 4336-43.
88. Da, B., D. Dawson, and T. Stearns, *Methods In Yeast Genetics: A Cold Spring Harbor Laboratory Course Manual.* 2000.
89. Bogdanova, E.A., et al., *Normalization of Full-Length-Enriched cDNA*, in *cDNA Libraries: Methods and Applications*, C. Lu, J. Browse, and J.G. Wallis, Editors. 2011, Humana Press: Totowa, NJ. p. 85-98.
90. Pertea, M., et al., *StringTie enables improved reconstruction of a transcriptome from RNA-seq reads.* Nature Biotechnology, 2015. **33**(3): p. 290-295.
91. Kolde, R., *Pheatmap: pretty heatmaps.* R package version, 2012. **1**(2): p. 726.
92. Liao, Y., G.K. Smyth, and W. Shi, *featureCounts: an efficient general purpose program for assigning sequence reads to genomic features.* Bioinformatics, 2013. **30**(7): p. 923-930.
93. Engel, S.R., et al., *The reference genome sequence of Saccharomyces cerevisiae: then and now.* G3 (Bethesda), 2014. **4**(3): p. 389-98.

94. Love, M.I., W. Huber, and S. Anders, *Moderated estimation of fold change and dispersion for RNA-seq data with DESeq2.* Genome Biology, 2014. **15**(12): p. 550.
95. Zhu, A., J.G. Ibrahim, and M.I. Love, *Heavy-tailed prior distributions for sequence count data: removing the noise and preserving large differences.* Bioinformatics, 2019. **35**(12): p. 2084-2092.
96. Blighe, K., S. Rana, and M. Lewis, *EnhancedVolcano: Publication-Ready Volcano Plots with Enhanced Colouring and Labeling. 2018 Available online: https://github. com/kevinblighe.* EnhancedVolcano (accessed on 14 December 2020).
97. Conway, J.R., A. Lex, and N. Gehlenborg, *UpSetR: an R package for the visualization of intersecting sets and their properties.* Bioinformatics, 2017. **33**(18): p. 2938-2940.
98. Cherry, J.M., et al., *Saccharomyces Genome Database: the genomics resource of budding yeast.* Nucleic Acids Res, 2012. **40**(Database issue): p. D700-5.
99. Khoshnevis, S., et al., *A conserved Bcd1 interaction essential for box C/D snoRNP biogenesis.* J Biol Chem, 2019. **294**(48): p. 18360-18371.
100. Weick, E.M., et al., *Helicase-Dependent RNA Decay Illuminated by a Cryo-EM Structure of a Human Nuclear RNA Exosome-MTR4 Complex.* Cell, 2018. **173**(7): p. 1663-1677 e21.
101. Schuller, J.M., et al., *Structure of the nuclear exosome captured on a maturing preribosome.* Science, 2018. **360**(6385): p. 219-222.
102. Oddone, A., et al., *Structural and biochemical characterization of the yeast exosome component Rrp40.* EMBO Rep, 2007. **8**(1): p. 63-9.
103. Kobayashi, N., et al., *Structure and functional analysis of the multistress response gene DDR2 from Saccharomyces cerevisiae.* Biochem Biophys Res Commun, 1996. **229**(2): p. 540-7.
104. Lacroute, F., *Regulation of pyrimidine biosynthesis in Saccharomyces cerevisiae.* J Bacteriol, 1968. **95**(3): p. 824-32.
105. Minard, K.I. and L. McAlister-Henn, *Isolation, nucleotide sequence analysis, and disruption of the MDH2 gene from Saccharomyces cerevisiae: evidence for three isozymes of yeast malate dehydrogenase.* Mol Cell Biol, 1991. **11**(1): p. 370-80.
106. Keesey, J.K., Jr., R. Bigelis, and G.R. Fink, *The product of the his4 gene cluster in Saccharomyces cerevisiae. A trifunctional polypeptide.* J Biol Chem, 1979. **254**(15): p. 7427-33.
107. Yamamoto, R.T., et al., *RRN3 gene of Saccharomyces cerevisiae encodes an essential RNA polymerase I transcription factor which interacts with the polymerase independently of DNA template.* Embo j, 1996. **15**(15): p. 3964-73.
108. Hall, C. and F.S. Dietrich, *The reacquisition of biotin prototrophy in Saccharomyces cerevisiae involved horizontal gene transfer, gene duplication and gene clustering.* Genetics, 2007. **177**(4): p. 2293-307.
109. Phalip, V., et al., *Characterization of the biotin biosynthesis pathway in Saccharomyces cerevisiae and evidence for a cluster containing BIO5, a novel gene involved in vitamer uptake.* Gene, 1999. **232**(1): p. 43-51.
110. Mörtl, S., et al., *Biosynthesis of riboflavin. Lumazine synthase of Escherichia coli.* J Biol Chem, 1996. **271**(52): p. 33201-7.
111. Rieger, K.J., et al., *A novel nuclear gene, CBT1, essential for mitochondrial cytochrome b formation: terminal processing of mRNA and intron dependence.* Current Genetics, 1997. **32**(3): p. 163-174.
112. Ellis, T.P., M.S. Schonauer, and C.L. Dieckmann, *CBT1 interacts genetically with CBP1 and the mitochondrially encoded cytochrome b gene and is required to stabilize the mature cytochrome b mRNA of Saccharomyces cerevisiae.* Genetics, 2005. **171**(3): p. 949-57.

FIGURE LEGENDS

Figure 1. Overview of pathogenic amino acid substitutions in the human cap and core structural subunits of the RNA exosome. (**A**) Schematic view of the human RNA exosome with nine structural subunits (EXOSC1-9), denoted as 1-9, and one catalytic subunit (DIS3). (**B**) The structure and organization of the RNA exosome is highly conserved across eukaryotes. A structural model of the human RNA exosome (left) [PDB 6D6Q] [100] and the *S. cerevisiae* RNA exosome (right) [PDB 6FS7] [101] are depicted with the core and cap subunits that are linked to RNA exosomopathy diseases labeled and color coded. (**C**) Domain maps are shown for EXOSC2, EXOSC3, EXOSC5 and EXOSC9. Both cap subunits, EXOSC2 and EXOSC3, are composed of three different domains: an N-terminal domain, a central putative RNA binding S1 domain, and a C-terminal putative RNA binding K homology (KH) domain. The “GxNG” motif identified in the KH domain of both cap subunits is boxed in orange. The GxNG motif may play a structural role as it is buried at the interface between the S1 and KH domains in the 3D structure of the cap subunits [102]. Both core subunits, EXOSC5 and EXOSC9, are composed of a singular PH-like domain. The position of the RNA exosomopathy disease-linked amino acid substitutions in the human subunits are depicted above the domain structures in red. Sequence alignments of the orthologs from *Homo sapiens* (*Hs*), *Mus musculus* (*Mm*) and *S. cerevisiae* (*Sc*), below the domain structures, reveal the high conservation of the residues altered in disease (in red) and the sequences flanking these residues (in gray). The amino acid substitutions generated in the Rrp orthologs for this study that correspond to the pathogenic amino acid substitutions are shown below the sequence alignments in red.

Figure 2. *S. cerevisiae* that model disease-causing EXOSC variants show growth defects.

The growth of cells lacking individual RNA exosome subunits indicated and expressing the corresponding wild-type or disease-modeled mutant RNA exosome gene were analyzed (**A**) by serially diluting and spotting cells onto solid -Leu media and (**B-C**) by growing in liquid media to measure doubling times, at 30°C and 37°C. *BY4741* cells were used as wild-type isogenic controls (labeled wild-

type). Other cells lack specific RNA exosome subunit genes and express a vector with Leu maker which allows the expression of the wild type (WT) or variant RNA exosome subunits or an empty vector (e.v.) from the endogenous gene promoters. Growth measurements in liquid media used technical and biological triplicates. Quantified doubling times for each sample were normalized to the value of the wild-type parental control samples at each temperature.

Figure 3. RNA-Seq analysis of RNA exosomopathy mutant yeast models reveal large and distinct transcriptomic changes in the *rrp4-G226D, rrp40-W195R* and *rrp46-L191H* cells.

(**A**) Violin plots showing the distribution of transcripts identified in differential analysis as significant ($p<0.05$) in each mutant compared to the corresponding wild-type control. The y-axis shows the Log2 Fold Change (LFC) for each transcript. The solid grey line demarcates a Fold Change of +1.5 or -1.5 (LFC=0.585 or -0.585). The dotted grey line marks a Fold Change of +2 or -2 (LFC=1 or -1). (**B, D, F**) Volcano plots of the differentially expressed transcripts and classification of RNA types in *rrp4-G226D, rrp40-W195R* and *rrp46-L191H* cells. (**C, E, G**) Stacked bar graph of the percentages of different RNA classes within the differentially expressed transcripts in *rrp4-G226D, rrp40-W195R* and *rrp46-L191H* cells. RNA classes are shown as percentages and include messenger RNAs (mRNA), small nuclear RNAs (snRNA), small nucleolar RNAs (snoRNA), transfer RNAs (tRNA), cryptic unstable transcripts (CUTs), stable unannotated transcripts (SUTs), other non-coding RNA (ncRNA; e.g., *TLC1*), pseudogenes, and uncharacterized or dubious open reading frames (ORFs). Vertical lines mark FC values of ±1.5 (straight line) and ±2 (dotted line). (**B**) Differential expression analysis of cells expressing *rrp4-G226D* compared to those expressing *RRP4*. (**C**) Stacked bar graph of the percentages of different RNA classes within the differentially expressed transcripts in *rrp4-G226D* cells. (**D**) Differential expression analysis of cells expressing *rrp40-W195R* compared to those expressing *RRP40*. (**E**) Stacked bar graph of the percentages of different RNA classes within the differentially expressed transcripts in *rrp40-W195R* cells. (**F**) Differential expression analysis of *rrp46-L191H* cells compared to cells expressing *RRP46*. (**G**) Stacked bar graph of the percentages of different RNA classes within the differentially expressed transcripts in *rrp46-L191H* cells.

Figure 4. UpSet Plots of differentially expressed transcripts in *rrp4-G226D, rrp40-W195R* and *rrp46-L191H* cells reveal shared targets involved in metabolism and rRNA processing. The UpSet plot of significantly increased (FC≥+1.5) (**A**) or decreased (FC≤-1.5) (**D**) transcripts within the *rrp4-G226D, rrp40-W195R* and *rrp46-L191H* datasets. Pie chart of the types of RNA that comprise the intersection of shared increased (Up) (**B**) or decreased (Down) (**E**) transcripts (Up). Gene ontology (GO) analysis for biological process of the shared increased (**C**) or decreased transcripts (**F**). The sets of samples are color coded; transcripts identified FC≤-1.5 or FC≥+1.5 from differential expression analysis of *rrp40-W195R* vs *RRP40* are colored blue; those of *rrp46-L191H* vs *RRP46* are colored red; and those of *rrp4-G226D* vs *RRP4* wild-type control cells are colored teal. Black bars in C and F represent the number of transcripts that are linked to each biological process category, whereas orange bars represent the -log of the associated *p*-value for each GO term. GO analyses were performed on coding (mRNA) and non-coding RNAs (tRNAs, snoRNAs, and snRNAs).

Figure 5. UpSet Plots of differentially expressed transcripts in *rrp4-G226D, rrp40-W195R* and *rrp46-L191H* cells reveal targets uniquely impacted. UpSet plots generated as in Figure 4. The intersections assessed here are transcripts significantly increased or decreased by 1.5-fold or more only in the *rrp40-W195R* dataset (blue), the *rrp46-L191H* dataset (red) or the *rrp4-G226D* dataset (teal). The UpSet plot of significantly increased (FC≥+1.5) (**A**) or decreased (FC≤-1.5) (**E**) transcripts occurring solely in the *rrp40-W195R* dataset, or the *rrp46-L191H* dataset, or in the *rrp4-G226D* dataset. Stacked bar percentages of the RNA types that comprise the increased (Up) (**B**) or decreased transcripts (Down) (**F**) identified only within the *rrp40-W195R, rrp46-L191H* or *rrp4-G226D* datasets. Gene ontology (GO) analysis for biological process of the increased (**C**) or decreased (**G**) transcripts occurring only in the *rrp40-W195R* dataset; increased (**D**) or decreased (**H**) transcripts occurring only in the *rrp46-L191H* dataset; and the decreased transcripts occurring only in the *rrp4-G226D* dataset (**I**). In panels C-D and G-I, black bars represent the number of transcripts that are linked to each biological process category,

whereas colored bars represent the -log of the associated *p*-value for each GO term. All GO analyses were performed on coding (mRNA) and non-coding RNAs (tRNAs, snoRNAs, and snRNAs).

Figure 6. Ribosome biogenesis and translation fidelity defects in *rrp4-G226D, rrp40-W195R* and *rrp46-L191H* mutant cells. (A) Northern blots reveal lower levels of 18S, 25S and 5.8S mature rRNAs and accumulation of precursor 7S rRNA in cells expressing *rrp40-W195R*, *rrp46-L191H*, and *rrp4-G226D* compared to their corresponding wild-type (WT) control. Data shows quantification of northern blots shown in Figure S5A for 2-3 independent biological replicates. (B) Dual-luciferase reporter assays to measure translation fidelity. The expression of firefly and Renilla luciferase was measured in cells expressing *rrp40-195R*, *rrp46-L191H*, and *rrp4-G226D* or the corresponding wild-type plasmids. The ratio of firefly luciferase to Renilla luciferase was normalized to the control plasmids. Four to twelve biological replicates were analyzed.

Figure 7. Distinct translation defects in *rrp4-G226D, rrp40-W195R* and *rrp46-L191H* mutant cells. (A) Sucrose density gradients of wild-type, *rrp40-195R*, *rrp46-L191H*, or *rrp4-G226D* cells that were grown 37°C are shown. Clarified cell extracts were resolved on a 10-50% sucrose gradient and scanned at 260 nm. Arrows indicate halfmers. (B-C) Northern blots of gradient fractions indicating distribution of 5.8S rRNA and 7S pre-rRNA. Samples in C were treated with 2.5 mM puromycin after lysis.

FIGURE 1

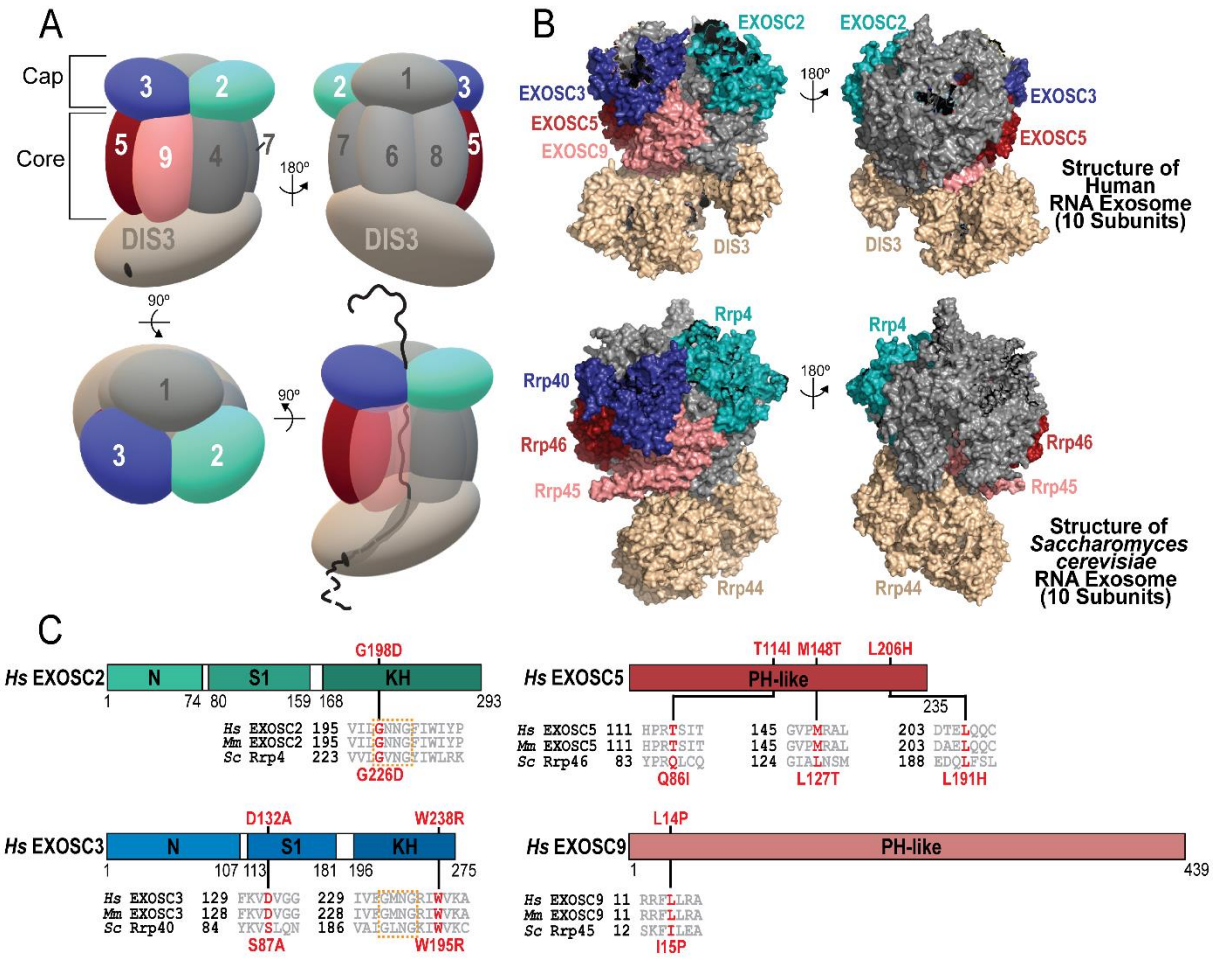

FIGURE 2

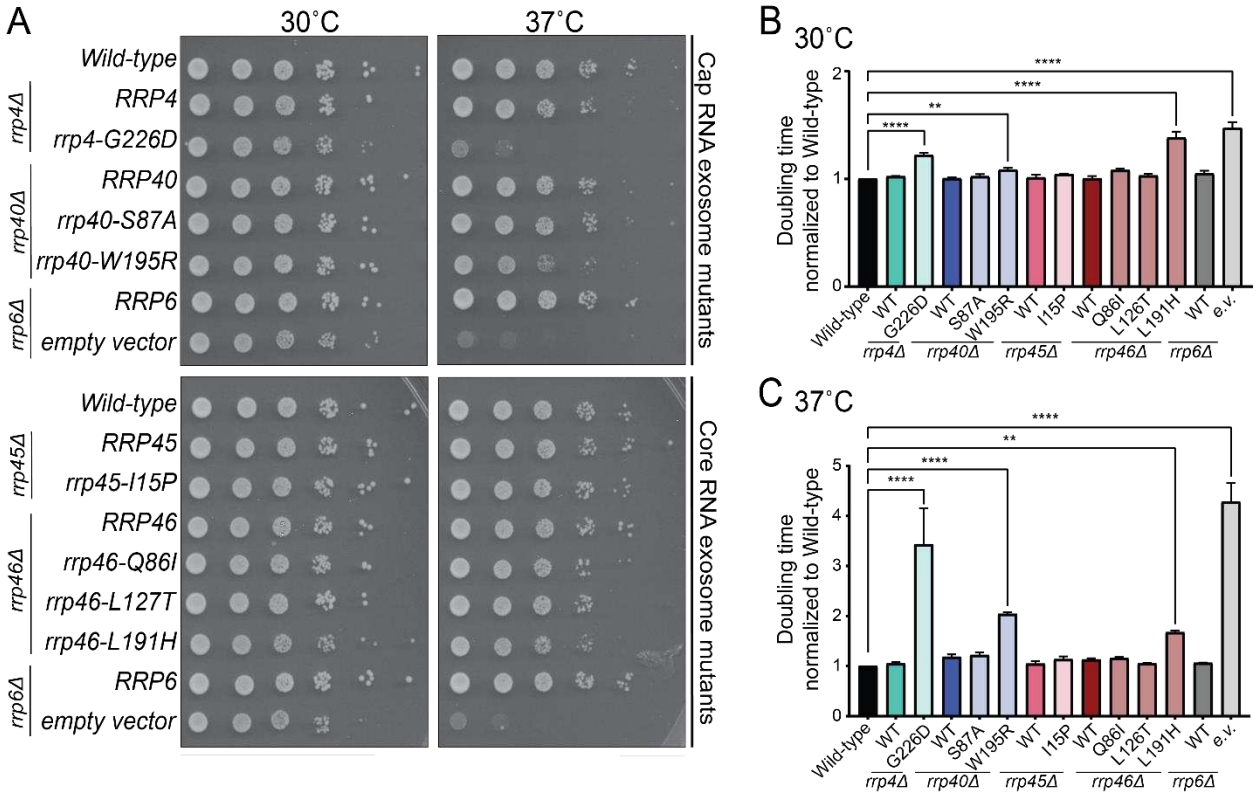

FIGURE 3

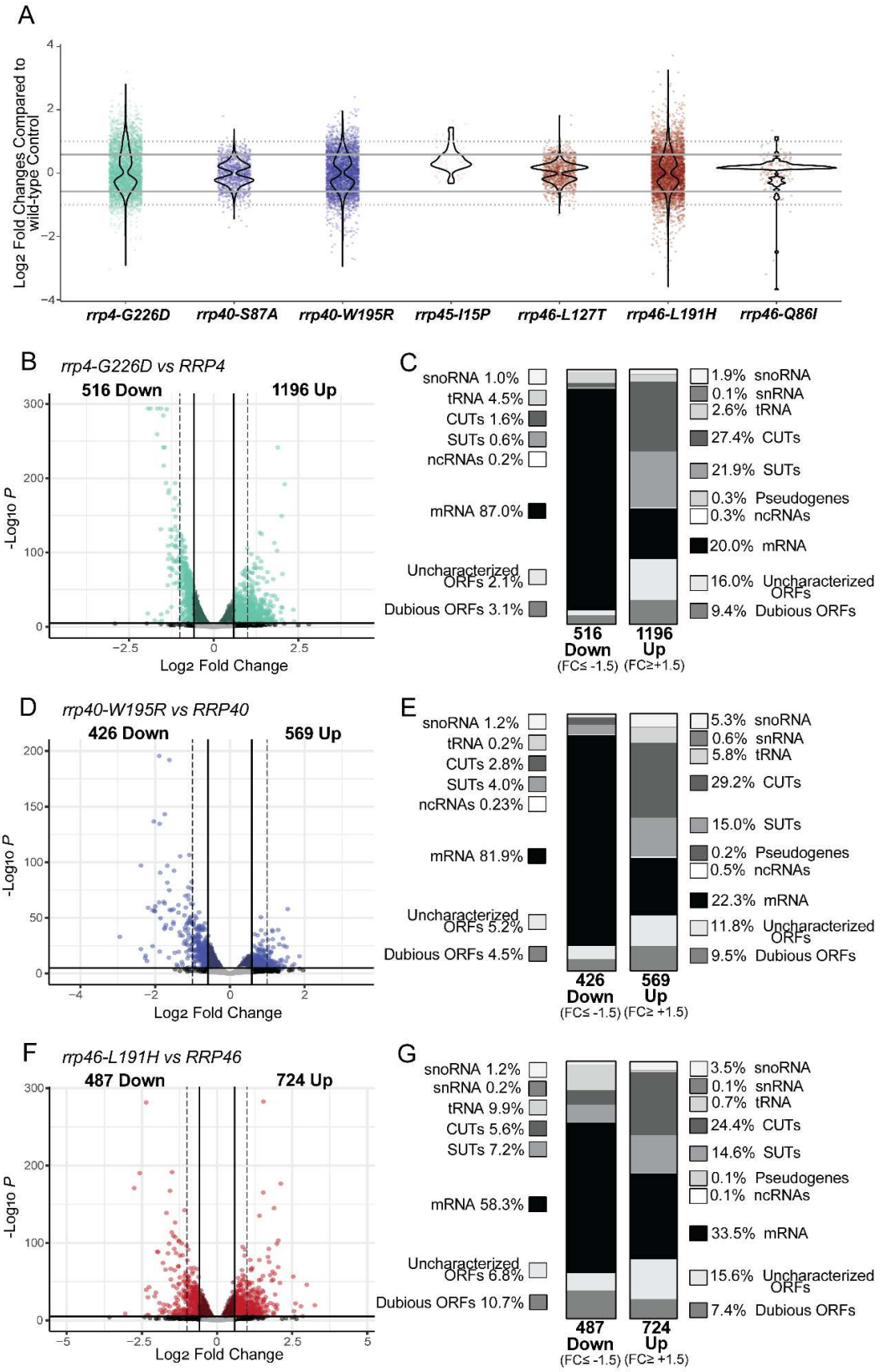

FIGURE 4

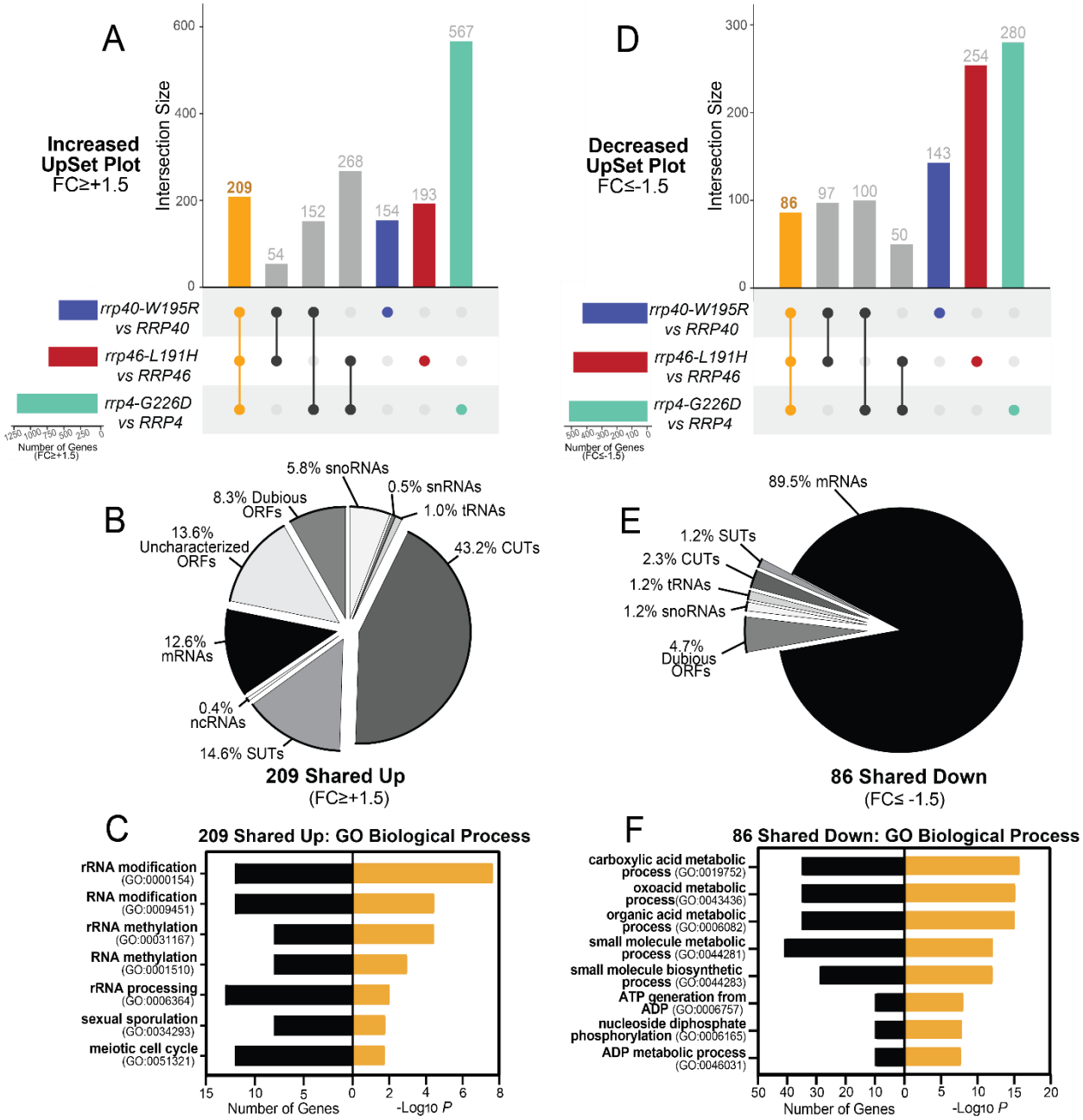

FIGURE 5

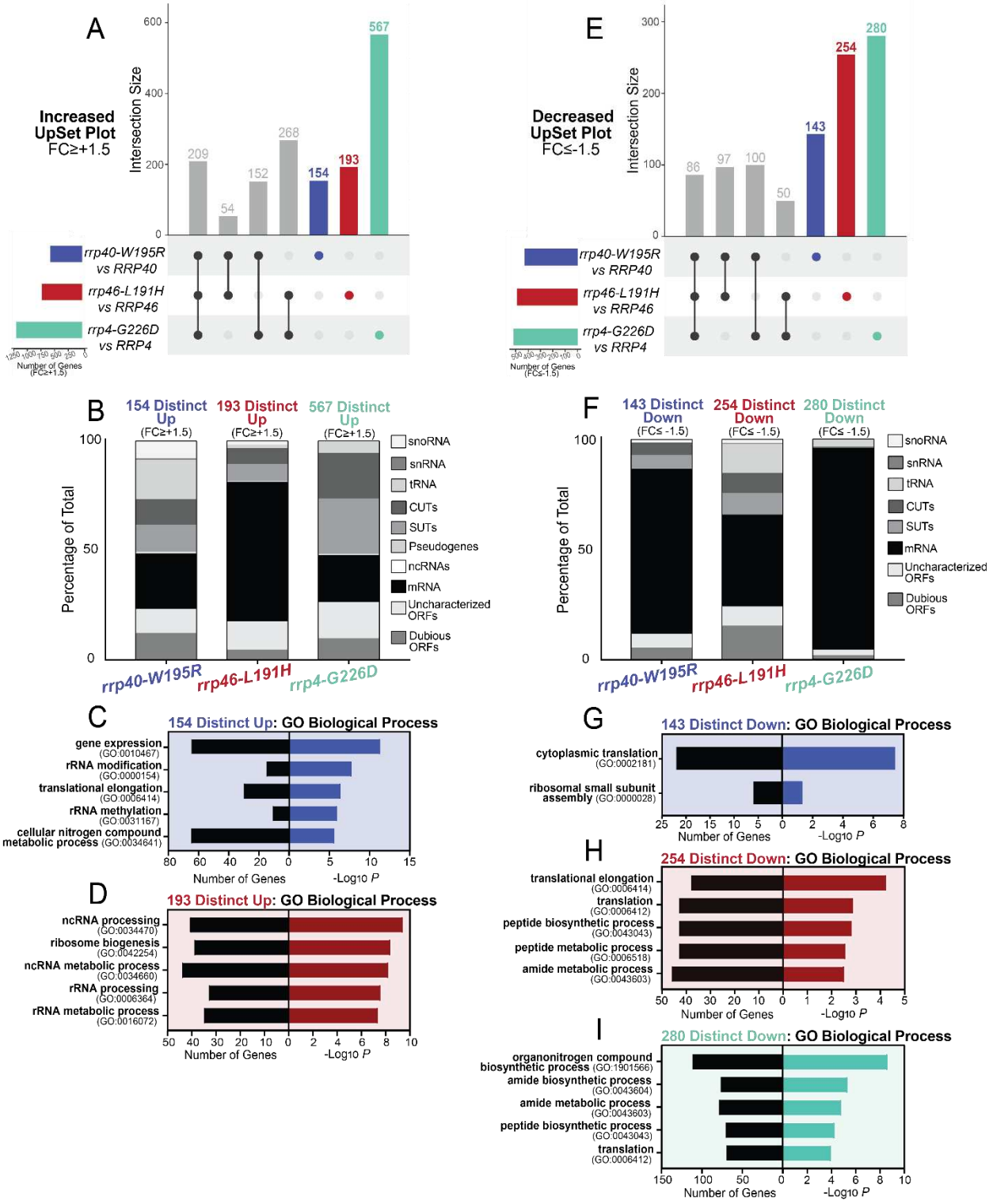

FIGURE 6

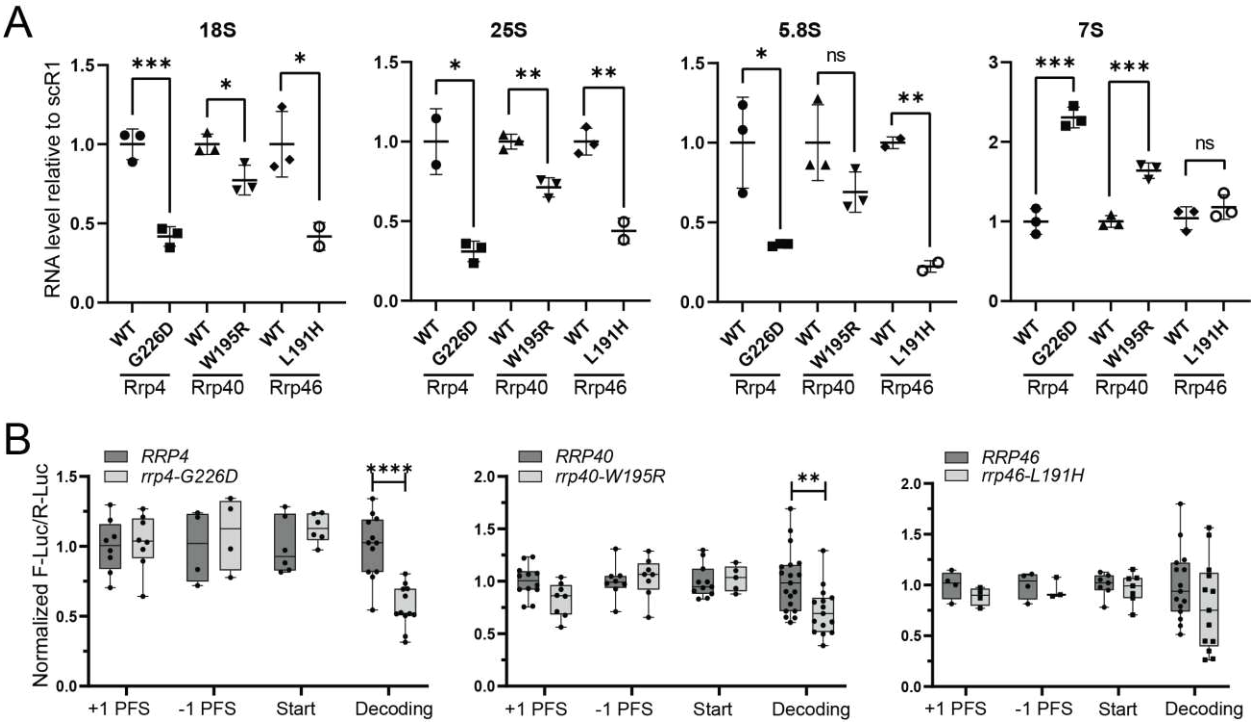

FIGURE 7